FINAL REPORT: FA9550-07-1-0136, Dec. 2006 – Nov. 2009

Development of Non-Equilibrium Plasma-Flame Kinetic Mechanism and its Validation Using Gliding Arc Integrated with Counterflow Burner

Principle Investigator: Yiguang Ju
Department of Mechanical and Aerospace Engineering
Princeton University
D330, Engineering Quadrangle, Olden Street
Princeton, NJ 08544
E-mail: yju@princeton.edu
Phone: 609-258-5644, Fax: 609-258-6233

Grant Number: **FA9550-07-1-0136**

Program Manager: Dr. Julian M. Tishkoff

Research Period: Dec. 2006 – Nov. 2009
Report date: Feb.21st, 2010

REPORT DOCUMENTATION PAGE

Form Approved
OMB No. 0704-0188

1. REPORT DATE *(DD-MM-YYYY)*	**2. REPORT TYPE**	**3. DATES COVERED** *(From - To)*
21-02-2010	Final	12-01-2006 – 30-11-2009

4. TITLE AND SUBTITLE
(U) Development of Non-Equilibrium Plasma-Flame Kinetic Mechanism and its Validation Using Gliding Arc Integrated with Counterflow Burner

5a. CONTRACT NUMBER

5b. GRANT NUMBER
FA9550-07-1-0136

5c. PROGRAM ELEMENT NUMBER
61102F

6. AUTHOR(S)
Ju, Yiguang; Ombrello, Timothy; Fridman, Alexander

5d. PROJECT NUMBER
2308

5e. TASK NUMBER
TA

5f. WORK UNIT NUMBER

7. PERFORMING ORGANIZATION NAME(S) AND ADDRESS(ES)

Princeton University
Department of Mechanical and Aerospace Engineering
EQUAD on Olden Street
Princeton, NJ 08544

Drexel University
Drexel Plasma Institute
34th Street and Lancaster Avenue
Philadelphia, PA 19104

8. PERFORMING ORGANIZATION REPORT NUMBER

9. SPONSORING / MONITORING AGENCY NAME(S) AND ADDRESS(ES)
AFOSR/NA
875 North Randolph Street
Suite 325, Room 3112
Arlington, VA 22203-1768

10. SPONSOR/MONITOR'S ACRONYM(S)

11. SPONSOR/MONITOR'S REPORT NUMBER(S)

12. DISTRIBUTION / AVAILABILITY STATEMENT
Approved for public release; distribution is unlimited

13. SUPPLEMENTARY NOTES

14. ABSTRACT

Kinetic enhancements of NO_x, O_3, and $O_2(a^1\Delta_g)$ on ignition and flame propagation of CH_4 and H_2, C_3H_8 and C_2H_4 flames by non-equilibrium plasma discharges in air were studied experimentally. The important kinetic enhancement pathways were identified. It was found that plasma produced NO_x played a dominant role in the reduction of ignition temperature, particularly at low temperatures and low stretch rates. Moreover, the results showed that NO_x catalytic effect mitigated the inhibiting effects of H_2O and CH_4 on ignition. A new method to isolate the kinetic coupling of O_3 and $O_2(a^1\Delta_g)$ was proposed and the kinetic enhancement of O_3 and $O_2(a^1\Delta_g)$ on flame speed was investigated quantitatively by using a lifted flame and advanced absorption and cavity ring down spectroscopy. It was found that O_3 decomposition in the early stages of the preheating zone produced atomic O which reacted rapidly with the fuel to extract chemical heat release to increase flame speed. It was also found that $O_2(a^1\Delta_g)$ formation enhance combustion considerably via $H+ O_2(a^1\Delta_g)=OH+O$ chain-branching reaction. The results will have a direct impact on the development of detailed plasma-flame kinetic mechanisms.

15. SUBJECT TERMS
Non-equilibrium plasma assisted combustion, Singlet oxygen, Ozone, NOx, Counterflow flame, Lifted flame

16. SECURITY CLASSIFICATION OF:			**17. LIMITATION OF ABSTRACT**	**18. NUMBER OF PAGES**	**19a. NAME OF RESPONSIBLE PERSON**
a. REPORT	**b. ABSTRACT**	**c. THIS PAGE**			Julian M. Tishkoff
Unclassified	Unclassified	Unclassified	UL	49	**19b. TELEPHONE NUMBER** *(include area code)* (703)696-8478

Table of Contents

Abstract ……...….2
1.0 Introduction.....3
2.0 Experimental Methods and Results of Non-Equilibrium Plasma-assisted Combustion .6
2.1 NO_x Catalytic Effects on Ignition Enhancement with Magnetic Gliding Arc (MGA) 6
2.1.1 Experimental System and Methods.....6
2.1.2. Computational Methods.....8
2.1.3. Results and Discussion 8
2.1.4. Conclusions.....13
2.2 Flame Propagation Enhancement by Plasma Generated O_3 14
2.2.1 Experimental System and Methods.....14
2.2.2 Quantitative Absorption Measurements of O_3.....16
2.2.3. Results and Discussion.....17
2.2.4. Conclusions.....25
2.3 Flame Propagation Enhancement by Plasma Generated $O_2(a^1\Delta_g)$.....26
2.3.1Experimental System.....26
2.3.2 Results and Discussion 31
2.3.3 Conclusions.....41
3.0 Participating Personnel.....42
4.0 Publications.....43
Peer Reviewed Journal Publications 43
Presentations at Conferences.....43
5.0 Interactions and Consultations 44
6.0 Honors and Awards.....44
7.0 Inventions.....44
8.0 References of This Report.....45

Abstract

Kinetic enhancements of NO_x, O_3, and $O_2(a^1\Delta_g)$ on ignition and flame propagation of CH_4 and H_2, C_3H_8, and C_2H_4 flames by non-equilibrium plasma discharges in air were studied experimentally. The important kinetic enhancement pathways were identified. Plasma-produced NO_x played a dominant role in the reduction of ignition temperature particularly at low temperatures and low stretch rates; moreover, the results showed that NO_x catalytic effect mitigated the inhibiting effects of H_2O and CH_4 on ignition. A new method to isolate the kinetic coupling of O_3 and $O_2(a^1\Delta_g)$ was proposed, and the kinetic enhancement of O_3 and $O_2(a^1\Delta_g)$ on flame speed was investigated quantitatively by using a lifted flame and advanced absorption and cavity ring down spectroscopy. O_3 decomposition in the early stages of the preheating zone produced atomic O which reacted rapidly with the fuel to extract chemical heat release to increase flame speed. Also, $O_2(a^1\Delta_g)$ formation enhanced combustion considerably via the $H+O_2(a^1\Delta_g)=OH+O$ chain-branching reaction. The results will have a direct impact on the development of detailed plasma-flame kinetic mechanisms.

1.0 Introduction

The development of high-speed air-breathing propulsion vehicles with scramjet engines has created the challenges of achieving efficient and reliable ignition, flame propagation, and flame stabilization. Particularly, when hydrocarbon fuels are used, the flow residence time is comparable to the chemical reaction time, and ignition and flame stabilization become extremely difficult; therefore, the development of new methods to decrease ignition delay time and to increase flame stabilization and flame propagation rates is critical for the development of vehicles capable of hypersonic flight.

One of the potential solutions to enhance combustion and chemical reactions is the application of plasma activation. Plasma-assisted combustion produces elevated temperatures, radicals, excited species, ions, and electrons that have the possibility to increase the rate of fuel oxidation. Because of the significant promise of plasmas, extensive research has been performed using a variety of plasma discharge systems, including plasma torches/jets [1,2,3,4], gliding arc discharges [5,6,7], fast ionization waves [8, 9], and nanosecond repetitively pulsed discharges [10, 11], as well as through electric field interactions [12,13,14,] and microwave discharges [15,16,17]. The investigations have shown that plasma can enhance combustion processes with decreased ignition time and lower ignition temperatures [6,7,10,11,18,19], increased flame propagation [13,14,16,17,20], and enhanced flame stabilization [2,3,7,15]. Despite many observations of plasma-assisted combustion, due to the complex kinetic and transport interaction there is a lack of data from controlled and well-defined experiments to advance the fundamental understanding of the kinetic processes [21].

One of the major challenges associated with understanding the plasma-flame interaction is to establish a well-defined experimental system to achieve the isolation of the effects of individual species and to gain a fundamental knowledge of specific enhancement processes. Plasma discharges can produce a wide range of stable and metastable species that have the potential to enhance combustion, especially when the discharge is in a premixture of fuel and oxidizer. There is a lack of understanding of what species and reaction pathways are the most important.

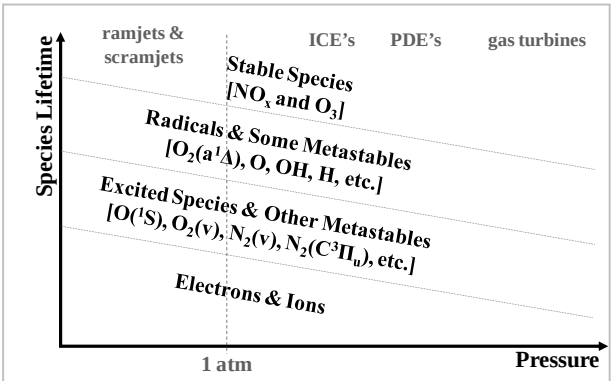

Fig.1 Lifetimes of plasma-produced species as a function of pressure in relation to common systems applications.

Figure 1 is an illustration of typical plasma-produced species and their lifetimes as a function of pressure in different engines. Depending upon the application and the species of interest, decoupling the plasma-flame interactions can be very challenging. For example, when the pressure is sufficiently low (sub-atmospheric), plasma-produced species have high mole fractions and long lifetimes. On the other hand, at extremely high pressures, plasma-produced species have very short lifetimes because of high rates of recombination and collisional quenching. Since the concentration of species is proportional to the pressure and hence the number density, the lower the pressure, the longer the mean free path and the lower the collision frequency. To minimize the loss of radicals and excited species, the pressures need to be low or the plasma discharge has to be created at the reaction zone to enhance combustion. Unfortunately, decoupling of the plasma-combustion interactions becomes increasingly difficult as the plasma

discharge is moved closer to the reaction zone. In addition, diagnostics of plasma-generated species in reaction zone is challenging. These complications make it difficult to elucidate the fundamental interactions, especially when trying to understand the effects of specific plasma-produced species.

Plasmas generate electrons, ions, excited species, radicals, and fuel fragments. The role of active radicals in combustion and plasma-assisted combustion has been studied extensively [19, 22]; however, the effects of long lifetime excited and intermediate species such as NO_x, O_3 and $O_2(a^1\Delta_g)$ are not well understood despite their great importance in affecting plasma-assisted combustion processes. The focus of this project is to understand the kinetic pathways of these species in affecting ignition and flame propagation of hydrocarbon fuels.

For the study of plasma generated NO_x effects on combustion, the extinction and ignition enhancements by NOx on hydrogen and methane diffusion flames were investigated by the PI using a counterflow flame integrated with a gliding arc [5, 6]. The results showed that plasma has a significant effect on the extension of the extinction limit; however, due to the fast recombination of radicals and the rich radical pool in flames, the effect of the plasma on flame extinction was predominately thermal. Experiments on hydrogen and methane ignition with plasma discharge in air demonstrated successfully that the production of NO in plasma reduced ignition temperature dramatically. Nevertheless, in practical combustion systems plasma discharges occur often under partially premixed conditions. As such, a question of how the kinetic inhibition of H_2O and CO_2 affects NO catalytic effects arises; therefore, the **first goal** of our research is to develop a simplified experimental apparatus to study partially premixed ignition in a plasma-flame system and use computational simulations to gain insight into the mechanisms of NO enhancement effects with the appearance of kinetic inhibition of H_2O and CO_2. A new experimental system was developed to study the non-thermal ignition of simple fueled (H_2-CH_4-air) counterflow diffusion flames by a non-equilibrium magnetic gliding arc (MGA) plasma discharge. Ignition temperatures were measured experimentally using air and ultra-lean pre-mixtures with H_2 and CH_4, and the concentrations of stable plasma-produced species were measured using an FT-IR spectrometer. These results were used, along with computational simulations, to identify some of the key species of non-thermal ignition enhancement in the plasma-flame system.

For the study of O_3 effects on combustion, there has been little experimental work emphasizing the combustion enhancement effects of O_3. Early experimental studies of the effects of O_3 on ignition delay times were conducted in compression and spark ignition engines [23,24,25,26,27]. Recently, laser ignition was investigated by using both CO_2 and KrF excimer lasers to excite and decompose O_3 [28,29,30]. To the authors' knowledge, there have only been two investigations of the effect of O_3 on flame propagation enhancement [25, 31]. Although these experiments reported flame speed enhancement by O_3, the exact mechanisms are not well understood. Moreover, quantification of the enhancement was difficult due to the complex experimental geometry; therefore, the **second goal** of the present work is to create a methodology to measure quantitatively the effects of plasma-generated O_3 on the enhancement of flame propagation at a pressure of 1 atm. In this project, the enhancement of flame propagation of C_3H_8 lifted flames by O_3 was investigated through the development of an integrated plasma-combustion experimental platform where the active species were produced, isolated, and transported, and quantitative measurements of O_3 were conducted by using absorption spectroscopy. The experimental results were compared to numerical simulations to

identify the important kinetic pathways of flame propagation enhancement in the plasma-flame systems.

Singlet delta oxygen, $O_2(a^1\Delta_g)$, which has a low excitation energy of 0.98 eV and long radiative lifetime (>4000 s) because of a spin-forbidden transition to the ground state [32], has attracted much attention because of the faster chain-branching rate of $H+O_2(a^1\Delta_g)$ than that of $H+O_2$. There have been numerous computational studies aimed to quantify the enhancement of ignition and flame stabilization by $O_2(a^1\Delta_g)$. Starik and Titova [33] showed that when O_2 was excited to its first electronic state of $O_2(a^1\Delta_g)$ by laser radiation in a supersonic flow of H_2-air, the induction time and temperatures necessary for ignition behind a shockwave were reduced significantly. They attributed the enhancement to come from new pathways with $O_2(a^1\Delta_g)$ to generate active species, such as O, H, and OH. Numerical simulations also were performed to demonstrate similar effects of $O_2(a^1\Delta_g)$ using an electrical discharge [34]. Detailed investigations of the ignition kinetics with the presence of $O_2(a^1\Delta_g)$ by non-equilibrium excitation in a H_2-O_2 system was reviewed by Popov [35]. The review pointed out that if the quenching of $O_2(a^1\Delta_g)$ by H_2 is not considered, there will be a gross overestimate of the amount of enhancement because the collisional quenching rate increases significantly with temperature. Popov also emphasized was that there is a lack of experimental studies of the effect of electronically excited species on combustion phenomena.

Starik, Kuleshov, and Titova studied the ignition enhancement of $O_2(a^1\Delta_g)$ and $O(^1D)$ in an H_2-O_2 mixture. The collective effect of these two species led to decreased ignition delay times by several orders of magnitude [36]. Kozlov, Starik, and Titova also conducted numerical simulations on ignition to show the enhancement of H_2-O_2 flame speed with $O_2(a^1\Delta_g)$ addition [37]. The results showed that a concentration of 10% $O_2(a^1\Delta_g)$ gave more than a 50% increase in the laminar flame velocity. Bourig et al. [38] extended the numerical modeling by investigating ignition and flame propagation, as well as flame stabilization by $O_2(a^1\Delta_g)$. Experimental validation of the enhancement of $O_2(a^1\Delta_g)$ on ignition was introduced by measurement of the emission from OH* at 306.4 nm [39]. The results of OH* measurements confirmed the kinetic enhancement by $O_2(a^1\Delta_g)$. Skrebkov and Karkach [40] performed subsequent simulations using the ignition and emission spectroscopy results and showed that there was reasonable agreement; however, they emphasized that the main stumbling block was the "availability of experimentally evaluated amounts of $O_2(a^1\Delta_g)$" [41].

To date, there has only been one experimental investigation of the effects of $O_2(a^1\Delta_g)$ on combustion phenomena. Smirnov et al. [42] performed experiments aimed at isolating the effect of $O_2(a^1\Delta_g)$ on the ignition of H_2-O_2-He mixtures at low pressure between 1.33 kPa and 2.67 kPa. The results showed decreased induction times. In order to isolate the effect of O and O_3, Hg and its oxide (HgO) were injected into the flow; however, the concentration of O_3 was not measured, and $O_2(a^1\Delta_g)$ was measured only through emission intensity. The measurements did not provide quantitative concentrations of all the major species of enhancement in the system, although it was the first attempt to isolate the effect of $O_2(a^1\Delta_g)$ and the results agreed reasonably well with their previous calculations [43,44]. In addition, the experiments were conducted only for a H_2-O_2 mixture. Collision quenching of $O_2(a^1\Delta_g)$ by hydrocarbon molecules were not considered; therefore, there are scarce experimental data quantifying the effect of electronically excited species, specifically $O_2(a^1\Delta_g)$, on combustion phenomena. A majority of the numerical and experimental work has been focused on the H_2-O_2 reaction system, with no experimental studies of the isolated effects of $O_2(a^1\Delta_g)$ on hydrocarbon based fuels; moreover, there have been no experimental studies at higher pressures, greater than 2.67 kPa, where a structured flame can

exist. Furthermore, there have been no experimental studies with quantitative and simultaneous concentration measurements of $O_2(a^1\Delta_g)$, O, O_3, and NO.

The **third goal** of the present work is to isolate and measure quantitatively the effects of $O_2(a^1\Delta_g)$ on the enhancement of flame propagation using a hydrocarbon-based fuel, as well as to understand the kinetic mechanisms involved. The enhancement of flame propagation speeds was investigated through the development of an integrated plasma combustion experimental platform, and absolute concentration measurements were taken through integrated cavity output absorption spectroscopy. The experiments provided the first experimental evidence of the isolated effect of $O_2(a^1\Delta_g)$ on the propagation of a hydrocarbon fuel-based flame. The results will provide important steps towards developing a comprehensive predictive model for plasma-combustion systems with detailed and well-defined experimental results.

2.0 Experimental Methods and Results of Non-Equilibrium Plasma-assisted Combustion

2.1 NOx Catalytic Effects on Ignition Enhancement with Magnetic Gliding Arc (MGA)

2.1.1 Experimental System and Methods

In this experiment, we used the non-equilibrium Magnetic Gliding Arc (MGA) (**Fig.2**) developed in our previous studies [5,6] to produce NO_x. The MGA is a special type of gliding arc discharge with non-equilibrium properties. The arc is established first as a thermal equilibrium plasma. It then elongates while it is rotated around by the Lorentz force from the magnetic field. During this process, the arc gains more non-equilibrium properties as it cools and more voltage is drawn from the power supply. The arc stabilizes and rotates at the largest gap along the electrodes, not reinitiating at the smallest gap because of passing through pre-ionized gas from the prior rotation. A time-integrated photo of the top of the MGA is shown in **Fig.2**. The benefit of the MGA is that it has both thermal equilibrium and non-equilibrium processes to produce heat, NOx, as well as radicals needed to enhance ignition in a combustion system.

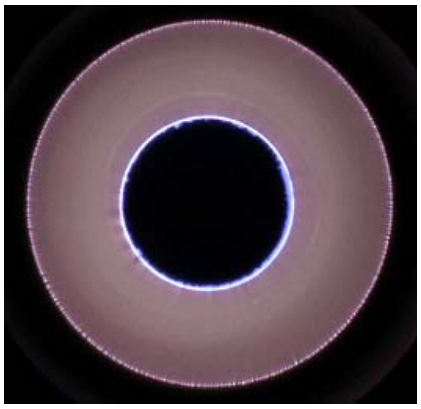

Fig.2 Time integrated photo of top view of MGA.

The MGA was integrated with a counterflow ignition system (**Fig.3**) because of the counterflow's unique benefits of simplified flame geometry, minimal buoyancy effects, and the ability to define a strain rate, a_i, (flow velocity gradient or inverse of residence time) on the centerline near the stagnation plane of the two impinging jets. The strain rate is defined as,

$$a_i = \frac{2v_i}{L}\left(1+\frac{v_j}{v_i}\sqrt{\frac{\rho_j}{\rho_i}}\right) \qquad (1)$$

where L, v and ρ are the length between the two nozzles, velocity, and density, respectively, and i and j are indices representing the two nozzles streams. The strain rate was a parameter used for comparison to computational simulations. A schematic of the MGA plasma discharge counterflow ignition system is shown in **Fig.3**. The ignition apparatus consisted of two converging nozzles opposed to each other. The upper nozzle was water-cooled and was used for N_2-diluted H_2. The lower nozzle was preceded with a silicon carbide heater to pre-heat the air, a spacer where small concentrations of H_2 and CH_4 were injected into the air stream to create ultra-

lean pre-mixtures, and finally the MGA plasma device. Both nozzles contained a N_2 co-flow to isolate the flame from any ambient air and disturbances.

The entire system was designed to measure steady-state ignition temperatures with and without plasma activation of air or ultra-lean pre-mixtures. The temperature profiles across the exit of the lower nozzle were confirmed to be peaked along the centerline with no hot spots in the flow; therefore, the ignition temperatures were measured with two different diameter K-type thermocouples axially at the exit of the lower nozzle. The two thermocouples could be interchanged at the same location in the flow, allowing for more accurate radiation and conduction corrections.

To achieve ignition in the system, the temperature of the oxidizer side initially was raised close to the ignition temperature. The temperature then was increased slowly in small increments by approximately 2 K - 3 K until ignition was achieved by increasing the power supplied to the silicon carbide heater. The heater power at which ignition occurred was recorded, and the flame was extinguished by closing off the supply of fuel. The heater power then was lowered, the fuel turned on, and the flow field correctly adjusted and optimized again. The heater power again was increased, ignition achieved, and power recorded. Once the power at ignition was found several times to be consistently the same, the fuel supply was closed off and the heater adjusted to that power. The thermocouples were placed in the flow axially at the exit of the lower nozzle, and the temperature was measured. This measured temperature was defined as the ignition temperature, and the procedure was followed several times to establish repeatability.

Any difference in ignition temperatures between having the MGA plasma discharge on and off would be a non-thermal effect because of the minimization of all localized thermal effects. The experiment therefore provided a well-defined system to study non-thermal ignition enhancement by a non-equilibrium plasma.

The significant distance between the MGA and the reaction zone yielded long residence time which would suppress any effects of ions or excited species and would focus on and isolate the effects of stable plasma-produced species. To quantify the stable plasma-produced species that affected the ignition of the H_2

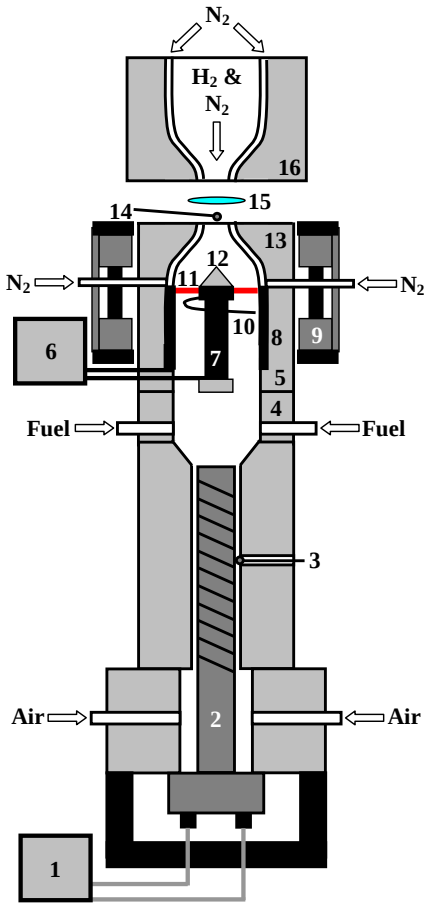

Fig.3 MGA Counterflow Ignition Apparatus 1. Silicon Controlled Rectifier, 2. Silicon carbide heater, 3. R-type thermocouple, 4. Fuel injection spacer 5. MGA plasma power supply, 5. MGA device, 6. MGA power supply, 7. Cathode, 8. Anode, 9. Magnets, 10. Gliding arc initiation wire, 11. MGA, 12. Insulator, 13. Nozzle with N_2 co-flow, 14. K-type thermocouple, 15. Diffusion flame, 16. Water-cooled nozzle with N_2 co-flow.

counterflow diffusion flames, a Fourier Transform Infrared (FT-IR) spectrometer was used. For accurate measurements of the stable species in the system, a 200 micron quartz probe was placed axially along the centerline at the exit of the lower nozzle where the thermocouples measured the peak temperature. The quartz probe was attached to the heated line of a Nicolet Magna-IR 550 Spectrometer. Pressure in the system was held constant at 336 Torr to ensure that the reactions would be quenched when pulled into the quartz sampling probe, as well as to maintain a high flow rate through the system to improve sampling time. The FT-IR was calibrated for six stable species which included CH_4, CO, CO_2, NO, NO_2 and H_2O at the same conditions of the experiments and in the appropriate concentration ranges.

2.1.2. Computational Methods

To validate the experimental results and understand the underlying mechanisms of ignition enhancement by the MGA, computational simulations were performed. A code derived from the PI's previously developed code for counterflow flame simulations was used. The S-curve response was found for all experimental conditions using the geometry of the actual counterflow burner and the species present at the exit of the nozzles. For the fuel side (upper nozzle), the species concentrations were held constant at 20% H_2 in 80% N_2, but for the oxidizer side (lower nozzle), the species ranged from a majority of air with 21% O_2 and 79% N_2 to small concentrations of plasma-produced species that were measured by the FT-IR, such as CH_4, CO, CO_2, NO, NO_2 and H_2O. Detailed chemistry was used with the mechanism of Li et al. [45] (H_2) and Mueller et al. [46] (NO_x) for the ignition with air and with ultra-lean H_2 pre-mixtures for the oxidizer side of the counterflow system. To capture the ignition phenomena correctly when using ultra-lean CH_4 pre-mixtures for the oxidizer side, the dimethyl-ether (DME) mechanism of Zhao et al. [47] was used with the NO_x of GRI-3.0 [48]. Zhao's DME mechanism aptly suited these cases because it had the H_2 sub-mechanism of Li et al., but also included CH_4 chemistry to capture the behavior of the species from the ultra-lean CH_4 mixtures. Furthermore, the DME mechanism of Zhao et al. had been validated by Zheng et al. for DME-blended CH_4-air flames [49]. The flame temperature versus strain rate S-curves were computed for the experimental conditions, and the ignition temperatures were found as a function of strain rate.

To identify the key species and reactions that were influential at ignition, a sensitivity analysis was performed at the ignition turning point on the S-curve. The sensitivity coefficient was defined as

$$SC = \frac{\partial \ln\left(a_{ignition}\right)}{\partial \ln\left(k_i\right)} \tag{2}$$

where $a_{ignition}$ was the strain rate at ignition and k_i was the reaction rate of the i^{th} reaction. A positive sensitivity coefficient meant that increasing the reaction rate accelerated ignition and vice versa.

2.1.3. Results and Discussion

To establish first a baseline set of experimental data, measurements of the ignition temperatures of only air as the oxidizer for the MGA being on and off was found, and the results are shown in **Fig.4**. The ignition temperatures decreased dramatically when the MGA was activating the air, indicating that there was significant non-thermal ignition enhancement by the plasma.

Since the oxidizer was only air, NO_x would be one of the few stable species capable of decreasing the ignition temperature. Quantitative measurements of NO_x were made using the FT-IR at the exit of the lower nozzle. Large concentrations of NO_x were found, with approximately 3500 parts per million (ppm) of NO and 1300 ppm of NO_2. The NO_x concentrations were used as initial/boundary conditions on the oxidizer side of the computational simulations. The computed curves of air and air with NO_x are shown in **Fig.4** with comparisons to the experimental results. There was good agreement when air was the oxidizer but an over-prediction of the enhancement by NO_x. The over-prediction was attributed to the fact that the NO_x input to the computation was only in the form of NO, not NO and NO_2. Since NO is a more effective catalyst than NO_2 in the NO_x cycle, the introduction of only NO to the simulations would yield lower ignition temperatures and hence an over-estimate of the ignition enhancement, which was observed. Overall, NO_x was the primary means of enhancement when only air was activated by the MGA.

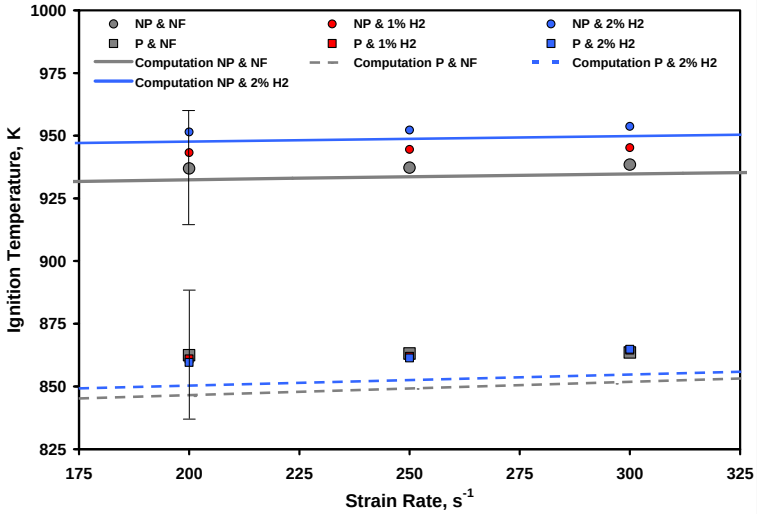

Fig. 4 H_2 counterflow diffusion flame ignition temperatures as a function of strain rate for air and ultra-lean H_2 pre-mixtures as the oxidizer with and without MGA plasma activation.

The results of a sensitivity analysis at the ignition turning points for the conditions of air and NO_x addition are shown in **Fig.5**. With the addition of NO_x, the ignition enhancement was from the catalytic role that the NO_x played on the oxidation of the inactive HO_2 radical by the reaction of

$$NO + HO_2 \Leftrightarrow NO_2 + OH \qquad R1$$

with the replenishment of NO from NO_2 coming mostly from the chain carrying reaction

$$NO_2 + H \Leftrightarrow NO + OH \qquad R2$$

and to a lesser extent by the reaction of

$$NO_2 + O \Leftrightarrow NO + O_2 \qquad R3$$

Figure 5 shows that there were other third body reactions that increased in importance with NO_x addition, but the net result was the conversion of HO_2 to two OH radicals. To understand the effect of other plasma-produced species, ultra-lean pre-mixtures were chosen in place of air as the oxidizer on the H_2 counterflow diffusion flames. The introduction of 1% and 2% H_2, as well as 0.2%, 0.5%, and 1% CH_4 downstream of the heater and upstream of the MGA, allowed for homogeneous ultra-lean pre-mixtures that were activated by the MGA.

Initially, measurements of the ignition temperatures using the ultra-lean H_2 pre-mixtures were taken and are shown in **Fig. 4** compared to no fuel addition. With the progressive increase of H_2 in the air, the ignition temperatures increased. Since the temperatures between the introduction of H_2 to the air and the exit of the nozzle were on the order of 1000 K, a majority of

the H_2 oxidized to H_2O. FT-IR spectrometer measurements confirmed that the majority of H_2 was converted to H_2O. Since H_2O is a very effective third body in the reaction

$$H + O_2 + M \Leftrightarrow HO_2 + M \qquad R4$$

converting the active H to HO_2, any H_2O present at the reaction zone would hinder ignition. Using the FT-IR spectrometer concentration measurements of H_2O in the counterflow code confirmed the ignition temperature rise, with good agreement to the experimentally measured temperatures (**Fig. 4**). Furthermore, the recent work of Langille et al. [50] showed similar results on counterflow H_2-air ignition using vitiated air. They found that for every 1% of H_2O addition there was approximately an 8 K rise in the ignition temperature, agreeing well with our results.

When the ultra-lean H_2-air pre-mixtures were activated by the MGA, the ignition temperatures did not change significantly from when only air was being activated. It was found by FT-IR spectrometer measurements that the concentration of H_2O at the exit of the lower nozzle decreased from that of no MGA activation; therefore, less H_2 was oxidized to H_2O. Computational simulations agreed well with the experiments and showed no appreciable change in the ignition temperature with H_2-air pre-mixtures in place of only air. Sensitivity analysis at the ignition limit on the S-curve showed that there were competing effects at ignition (**Fig. 5**). Less H_2O yielded higher ignition temperatures, but the significant concentrations of NO_x produced by the plasma oxidized the HO_2 (reaction R1) produced by the third body reaction, R4. Overall, the net effect was no significant change in the ignition temperature, which agreed well with the experimental results.

The most important result from using ultra-lean H_2-air pre-mixtures was that H_2O was a significant inhibitor of ignition, but when the MGA plasma activated the ultra-lean pre-mixtures,

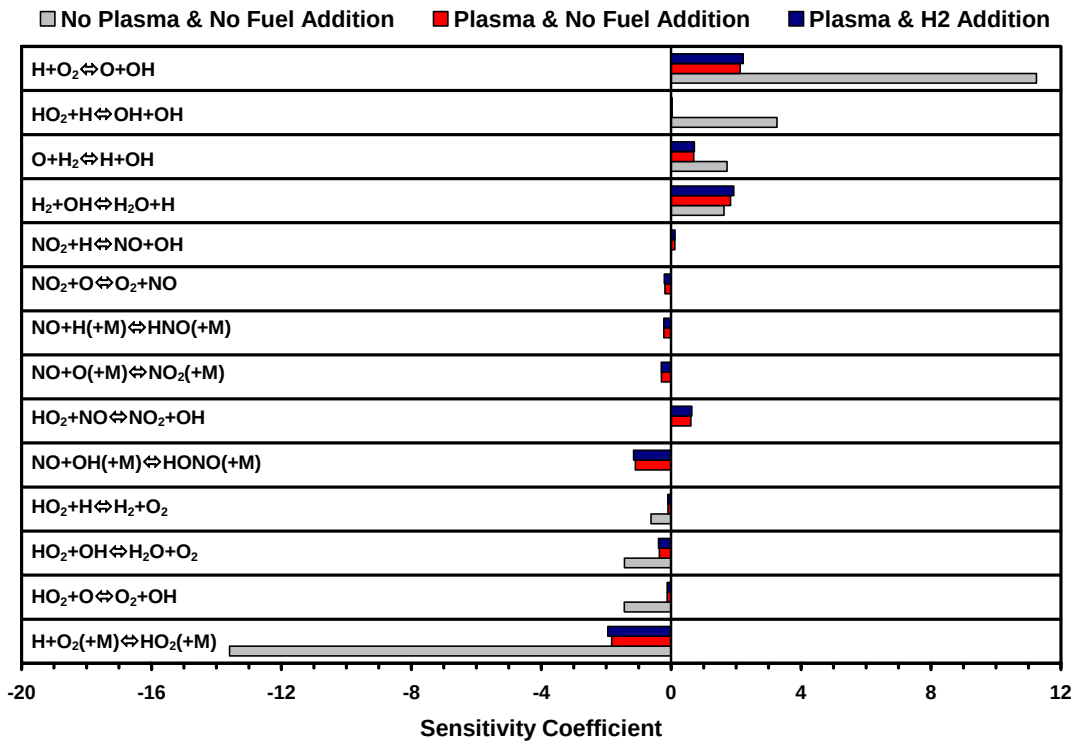

Fig.5 Sensitivity coefficients at ignition with and without MGA plasma activation of air and ultra-lean H_2 pre-mixtures as the oxidizer.

the effect was mitigated because of the NO_x production. Furthermore, the thermal oxidation in the oxidizer stream, which was the case for no MGA activation, the flow residence times and temperatures were crucial for any change in the chemical composition of the gas. When the MGA was used, the residence times and high temperatures were both lower, but significant conversion of the fuel was achieved. The results demonstrated the unique benefit of using a non-equilibrium plasma to create species for ignition enhancement and mitigate the effect of H_2O.

Different behavior was observed when using ultra-lean CH_4-air pre-mixtures for the oxidizer side of the H_2 counterflow diffusion flame ignition system. Firstly, for no MGA activation at low strain rates (a = 200 s^{-1}) the ignition temperatures increased much less than at higher strain rates (**Fig.6**). Unlike H_2, the flow residence times between the introduction of CH_4 to the air stream and the reaction zone were on the order of the ignition delay times of CH_4 at the associated gas temperatures. At low strain rates, there was sufficient time to oxidize fully the CH_4 to CO_2 and H_2O. FT-IR spectrometer measurements further confirmed the full oxidation of CH_4. In addition, numerical simulations showed that the majority of the ignition inhibition came from H_2O with CO_2. The residence time somewhere between the strain rates of 200 s^{-1} and 250 s^{-1} was on the order of the ignition delay time of CH_4 because more for the same amount of CH_4 addition, the ignition temperatures increased more at higher strain rates. To show this clearly, a dotted line was used to connect the computational results at the strain rates of 200 s^{-1} and 250 s^{-1} (**Fig.6**). The FT-IR spectrometer measurements confirmed that only a portion of the CH_4 was oxidized, with significant concentrations of CO, CO_2 and H_2O also present. When the concentrations from the experiments were used as inputs to the computations, there was good agreement with the measured ignition temperatures. A sensitivity analysis (**Fig.7**) showed that the significant increase in the ignition temperature was due predominately to the un-oxidized CH_4 converting the active OH radicals to H_2O through the reaction

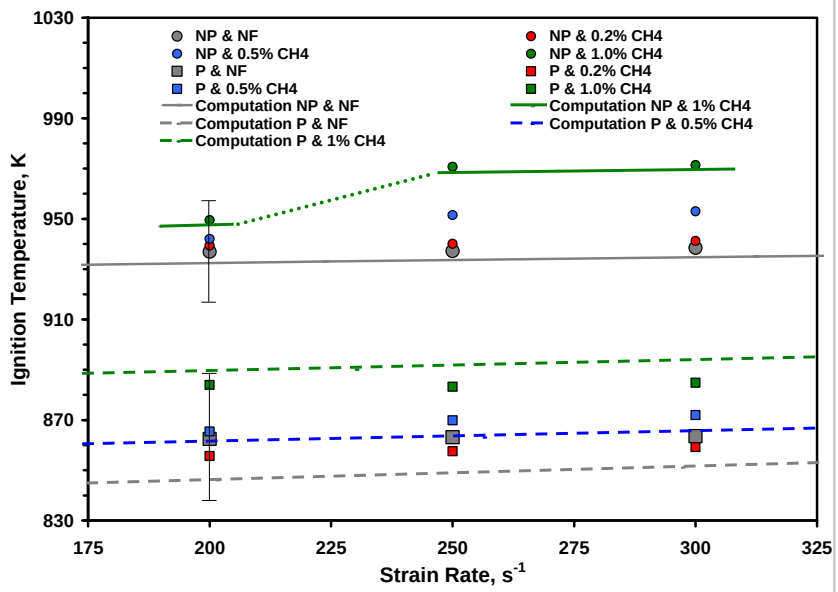

Fig.6 H_2 counterflow diffusion flame ignition temperatures as a function of strain rate for air and ultra-lean CH_4 pre-mixtures as the oxidizer with and without MGA plasma activation.

$$CH_4 + OH \Leftrightarrow CH_3 + H_2O. \quad \text{R5}$$

Other reactions of CH_4 and CH_3 with O and H competed with the branching reactions for H_2 oxidation of

$$H + O_2 \Leftrightarrow O + OH \quad \text{R6}$$

$$O + H_2 \Leftrightarrow H + OH \quad \text{R7}$$

to inhibit ignition but were far less important than reaction R5.

Unlike the MGA activated ultra-lean H_2 pre-mixtures, there was a significant change in the ignition temperatures for the MGA activated ultra-lean CH_4 pre-mixtures. The experimentally measured ignition temperatures are shown in **Fig.6**. There was a non-monotonic behavior observed with the increase of CH_4 in the oxidizer. The ignition temperatures decreased first with 0.2% CH_4 addition and then increased with 0.5% and 1% CH_4 addition to the oxidizer. To examine and understand the differences in ignition behavior, FT-IR spectrometer measurements of CH_4, CO, CO_2, NO, NO_2, and H_2O were taken. The concentrations of plasma-produced NO and NO_2 did not change with the addition of CH_4. Therefore, the rise in ignition temperature with increased CH_4 addition to the oxidizer was not caused by the change of NO_x. The FT-IR measurements did show that a significant portion of the CH_4 was oxidized to CO, CO_2, and H_2O. Unfortunately, the inhibition of ignition due to the presence of CO_2 was found to be minimal, on the order of a few Kelvin. The presence of H_2O only would increase the ignition temperature approximately a few Kelvin per 1 percent H_2O addition, which alone would not account for the up to 20 K rise of ignition temperatures that were observed. Furthermore, the concentrations of CO also would not change the ignition temperatures enough to match what was found experimentally; therefore, the unoxidized CH_4 had to account for the changes in the ignition temperature.

Computational simulations were performed first with the concentrations of CH_4, CO, CO_2, NO, NO_2 and H_2O measured by the FT-IR spectrometer and then were compared to the results of only CH_4, NO, and NO_2 addition. With the exclusion of CO, CO_2, and H_2O, the ignition temperatures changed only by a few Kelvin when compared to having all the species introduced. This result proved that ignition was very sensitive to the concentrations of CH_4 present. Sensitivity analysis for the two cases of 0.5% CH_4 and 1% CH_4 are shown in **Fig.8**. Once again, the CH_4 was responsible for consuming the active radicals of OH by reaction R5, with the additional reaction of

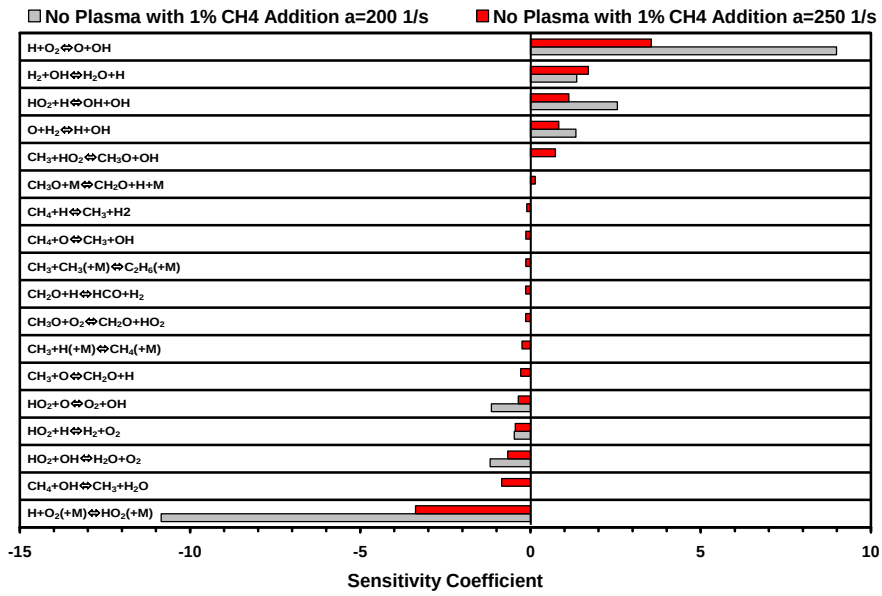

Fig.7 Sensitivity coefficients at ignition with and without MGA plasma activation of air and ultra-lean CH_4 pre-mixtures as the oxidizer.

$$CH_4 + H \Leftrightarrow CH_3 + H_2 \qquad R8$$

becoming important with increased CH_4 addition. For 0.2% CH_4 addition, none of the stable species measured by the FT-IR led to decreased ignition temperatures, hence more ignition enhancement. The under-prediction of ignition enhancement leaves open the possibility of the presence of other species that were not detected by the FT-IR that could enhance ignition further beyond what NO_x did. The possibility of other stable species, such as H_2, that cannot be measured because it does not absorb in the infrared, but more likely is the possibility of unstable or intermediate species that reached the reaction zone to enhance ignition, such as H, OH, O, etc., since small concentrations would yield significant results. Further investigation using different ultra-lean pre-mixtures with different concentrations of fuels would help to illuminate the possibility of these intermediate species leading to ignition enhancement.

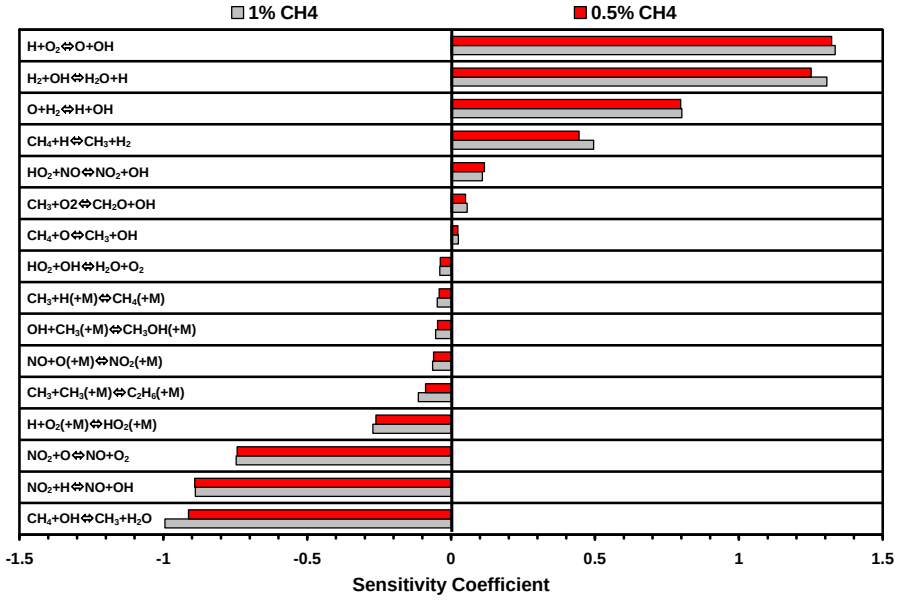

Fig.8 Sensitivity coefficients at ignition with MGA plasma activation of ultra-lean CH_4 pre-mixtures as the oxidizer.

2.1.4. Conclusions

The present work isolated and identified the key non-thermal ignition mechanisms when using a non-equilibrium MGA plasma discharge of air, H_2-air, and CH_4-air ultra-lean pre-mixtures as the oxidizer of H_2 counterflow diffusion flames. Identification of the non-thermal ignition mechanisms came from comparisons of experimental measurements of ignition temperatures, FT-IR spectrometer measurements of stable plasma-produced species, and computational simulations, including sensitivity analysis to identify the key reactions and species at ignition. Without MGA activation of the oxidizer, the ultra-lean H_2 and CH_4 cases showed the inhibition of ignition by H_2O and CH_4 by consuming active radicals. With MGA activation, there was a significant decrease in the ignition temperature, with NO_x being the primary species causing enhancement when air was the oxidizer. With ultra-lean H_2-air pre-mixtures as the oxidizer, no net change was observed in the ignition temperatures because of the NO_x mitigating the effect of H_2O by consuming the inactive HO_2 radical to produce active OH radicals. With MGA activation of the ultra-lean CH_4 pre-mixtures, the ignition temperatures increased significantly. The primary species that inhibited ignition was unoxidized CH_4, with the ignition temperature being extremely sensitive to the concentration of CH_4. Furthermore, the decreased

ignition temperatures for 0.2% CH_4 addition opens up the possibility of the presence of radicals or intermediate species that enhanced ignition. Overall, the MGA was able to mitigate the inhibiting effects of CH_4 on the ignition process because of the significant oxidation of CH_4 to CO, CO_2, and H_2O for all strain rates, as well as the large concentrations of ignition enhancing NO_x that was produced; therefore, to observe the maximum ignition enhancement of H_2 with the presence of CH_4, a non-equilibrium plasma should produce large concentrations of NO_x and oxidize as much of the CH_4 as possible because of the extreme sensitivity to its concentrations.

2.2 Flame Propagation Enhancement by Plasma Generated O_3

2.2.1 Experimental System and Methods

A laminar lifted flame burner was adopted for the combustion platform and used at a pressure of 101.3 kPa for all experiments. A schematic of the platform is shown in **Fig. 9**. The lifted flame burner consisted of a central fuel jet with an inner diameter of 0.271 mm that was located in a 90 mm inner diameter fused silica (quartz) tube to contain the co-flow of oxidizer. The fuel nozzle was shaped aerodynamically to produce a uniform velocity profile at the exit. The large ratio of diameters between the oxidizer co-flow and the fuel jet (>100) was used to ensure accurate comparisons to similarity solutions of the flow field. To ensure that the co-flow was uniform, two stainless steel meshes coated with silica for chemical inertness were separated by 3 cm and were located between the oxidizer inlet of the burner and the fuel jet exit. The gases used in the experiments were C_3H_8 for the fuel and ultra-high purity O_2 (99.99%) and N_2 (99.95%) mixed for the oxidizer. The flow rate of the fuel was controlled with a calibrated mass flow meter, while the O_2 and N_2 were controlled with calibrated sonic nozzles. The undiluted ultra-high purity O_2 was passed through a dielectric barrier discharge device and then was merged with the N_2 stream to be introduced to the lifted flame burner. This configuration minimized any problems of NO_x being produced in the discharge that would contaminate the flow. The dielectric barrier discharge device was comprised of a 110 mm long and 18 mm diameter co-axial sleeved tube geometry with a gap distance of 2 mm. The power was supplied by pulses of 3 kV to 10 kV positive and negative polarities with duration of 10 ns at FWHM with a frequency between 10 kHz and 40 kHz to produce different O_3 concentrations. Each pulse contained between 0.1 mJ and 1 mJ, providing between 1 W to 40 W total power. The discharge produced multiple oxygen-containing species, including O, O_3, $O_2(v)$, $O(^1D)$, $O(^1S)$, $O_2(a^1\Delta_g)$, $O_2(b^1\Sigma_g)$, etc.. To ensure that O_3 was the only species present in the flow when merged with the N_2 stream, a sufficient residence time

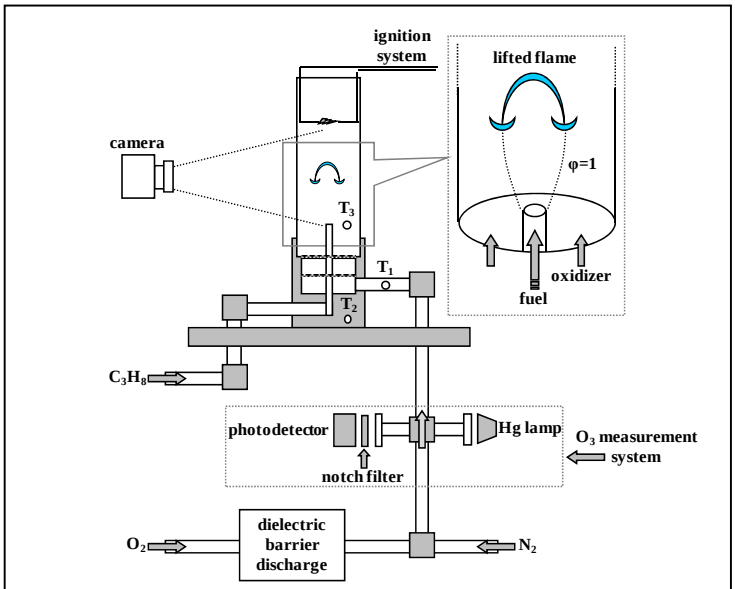

Fig. 9 Experimental set-up schematic of the lifted flame burner integrated with a dielectric barrier plasma discharge device and O_3 absorption measurement system.

was given to quench all plasma-produced species other than O_3. For example, **Table 1** lists the quenching rates of some of the common plasma-produced oxygen species. The atomic oxygen rapidly recombines with O_2 to produce O_3, which is stable. The next longest lived species is $O_2(a^1\Delta_g)$, which is metastable, and at 101.3 kPa and 300 K has a collisional lifetime of approximately 20 milliseconds. With the flow rate and length of the tube between the dielectric barrier discharge and the merging with N_2, the residence time was over 100 milliseconds; therefore, when the dielectric barrier discharge was supplied with power, the only change in the gases entering the combustion system would be the addition of O_3.

Reaction	**Reaction Constant [cm^3/molecule/s]**
$O+O_2+M \rightarrow O_3+M$	$6.0x10^{-34}$ = (HP limit $3.61x10^{-10}$)
$O(^1D)+O_2 \rightarrow O+O_2$	$4.0x10^{-11}$
$O_2(v)+O_2 \rightarrow O_2+O_2$	$1.73x10^{-13}$
$O_2(b^1\Sigma_g)+O_2 \rightarrow O_2+O_2$	$4.1x10^{-17}$
$O_2(a^1\Delta_g)+O_2 \rightarrow O_2+O_2$	$1.6x10^{-18}$
$O_2(a^1\Delta_g)+Ar \rightarrow O_2+Ar$	$1.0x10^{-20}$

Table 1 Reaction rates of plasma-produced oxygen species at 298 K. The term “HP” refers to the high pressure limit.

The high velocity fuel jet (3.5 – 10 m/s) and low velocity oxidizer co-flow (0.049 m/s) created a flow field with a stoichiometric contour where the premixed flame head of a lifted flame was located (shown in the top right insert in **Fig. 9**). The lifted flame, which also is called a tribrachial (triple) flame, had a premixed flame head anchored on the stoichiometric contour, followed by a diffusion flame tail. Direct photographs of the flame at various liftoff heights are shown in **Fig.10**. The lifted flame could be located at different stationary distances from the fuel jet nozzle depending upon the local flow velocity. For a fixed flow field, the flame was located in a stationary position where the lifted flame speed at the premixed flame head was balanced with the local flow velocity. If the flame speed increased, the liftoff height decreased to re-establish a local dynamic balance between the flame speed and flow velocity.

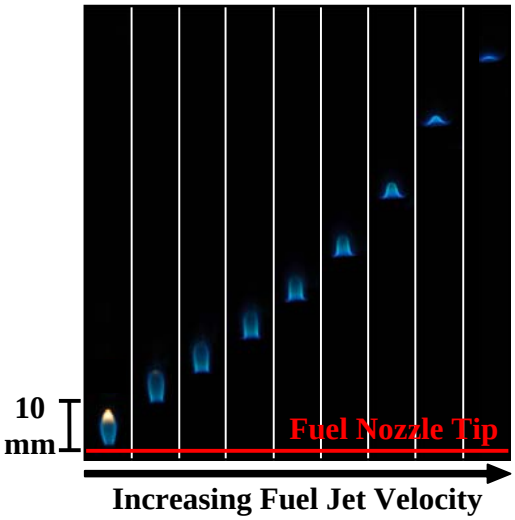

Fig. 10 Photographs of lifted flames at stationary positions for different fuel jet velocities.

A plot of the flame liftoff height versus fuel jet velocity is shown in **Fig. 11**. Due to the slow laminar boundary layer development and the velocity and concentration gradients created, the lifted flame height is very sensitive to the changes in flame speed and therefore provides excellent flame geometry for the direct observation of flame speed enhancement. For example, with only a small concentration of O_3, the flame liftoff height changes appreciably, as shown in **Fig. 11**. Since the fuel and oxidizer are not mixed far upstream of the flame, there is a very short residence time for the fuel and oxidizer to react in the cold flow. The short residence time helps to decouple the enhancement effects further, to be directly from reactions in the flame zone and not far upstream in the cold unreacted flow.

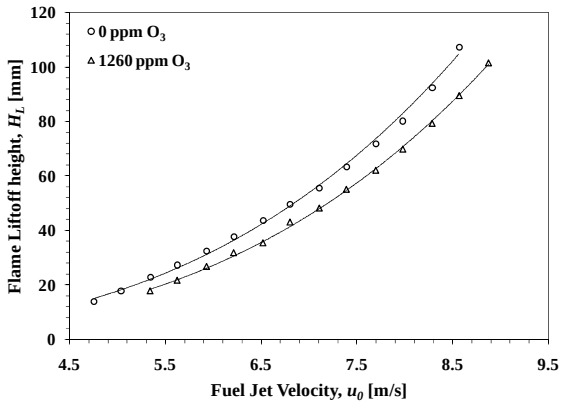

Fig. 11 Measurements of the flame liftoff height as a function of fuel jet velocity showing different flame stabilization locations from **Fig. 10**, as well as the sensitivity of flame speed changes.

Multiple temperatures were monitored by thermocouples placed on flow surfaces and in the flow and were recorded in the system. Temperatures were measured at points T_1, T_2, and T_3, shown in **Fig. 9**, and were, respectively, the burner inlet tube surface temperature, burner surface temperature, and co-flow gas temperature. Throughout the experiments, the temperatures remained constant within 0.2 K between the plasma being turned on and off.

2.2.2 Quantitative Absorption Measurements of O_3

The O_3 produced by the dielectric barrier discharge was measured using a one-pass, line-of-sight absorption cell in the flow downstream where the O_2 and N_2 streams merged. The absorption cell was comprised of a stainless steel compression cross fitting, with the side arms made of quartz tubes capped with UV quality windows. The cell was placed in the flow between the merging of the O_2 and N_2 streams and the burner. At one window, a mercury light with stable output provided ultraviolet light at the wavelength of 253.7 nm, where O_3 has a peak absorption cross section of 1.137×10^{-17} cm^2 (at 300 K) in the Hartley band [51]. A 10 nm notch filter (isolating only the 253.7 nm mercury line) and a photodiode detector were placed at the exit of the transmission cell. No other species present in the flow (O_2 and N_2) absorb at this wavelength; therefore, the change in the transmittance of the cell with the plasma on and off could be used to determine the O_3 concentration through the Beer-Lambert law

$$N_{ozone} = \frac{-\ln\left(\frac{I}{I_0}\right)}{\sigma_{ozone} L}. \quad (3)$$

where N_{ozone} is the absolute number density of the absorbing species, O_3, I the intensity of light with the presence of O_3, I_0 the intensity of light without the presence of O_3, σ_{ozone} the absorption cross section of O_3 at the excitation wavelength of 253.7 nm, and L the path length in the absorption cell (12.48 cm). The concentration then was calculated in parts per million (ppm) of O_3 with an uncertainty of approximately ± 2% and a minimum detectable threshold of

approximately 15 ppm. The uncertainty and minimum detectable threshold came from the fluctuations in the intensity of the mercury light as a function of time during the experiments.

The O_2 loading was fixed at 18% O_2 in 82% N_2 for the oxidizer co-flow. This O_2 loading was chosen to ensure that the flame was completely within the laminar flow regime for the 0.271 mm diameter fuel nozzle used [52], as well as to maintain a maximum liftoff height well below the location of the igniter. The oxidizer co-flow velocity was fixed at 0.049 m/s, and the fuel velocity was small enough to have a nozzle-attached diffusion flame when ignited. The flame was photographed using a high resolution (10.2 megapixel) Nikon D40x camera. Then the dielectric barrier discharge was turned on, and a photograph was taken again of the stationary flame. The fuel velocity then was increased in small increments. At each increment photographs were taken of the flame with the dielectric barrier discharge off and on. This procedure was executed for at least ten flame liftoff heights between a nozzle-attached flame and a flame at the top of the stoichiometric contour. The experimental repeatability of flame liftoff height as a function of fuel jet velocity was tested carefully multiple times. The results showed that the lifted flame co-flow system had deviations in the flame liftoff height that were negligibly small at less than 1 mm.

For each condition where the dielectric barrier discharge was on, the O_3 concentration was measured in the absorption cell. To ensure that the O_3 measured in the absorption cell was the concentration that was present at the flame front, the experiments were performed with the absorption cell at different distances and flow residence times between the merging of the O_2 and N_2 and measuring location, as well as between the measuring location and the flame. There was no change in the O_3 concentration measured and/or a change in the flame enhancement by O_3, confirming that the O_3 concentration measured in the absorption cell was the concentration present at the flame.

2.2.3. Results and Discussion

The lifted flame was established for fixed oxidizer co-flow velocity and O_2 loading (18% O_2 in 82% N_2). The fuel jet velocity was increased, and pictures were taken at each stationary flame condition with and without O_3 present in the oxidizer (**Fig. 9**). More than ten fuel jet velocities were chosen to give a complete data range between a nozzle-attached flame and blowout of a lifted flame at the top of the stoichiometric contour. Since the fuel jet velocity was almost a factor of 100 larger than the co-flow velocity and the fuel jet diameter was more than 100 times smaller than the co-flow diameter, a similarity solution was applicable for the cold flow. The similarity solution was used to find where the stoichiometric contour existed and hence where the premixed head of the lifted flame was anchored.

By accounting for the density, the virtual origin, and co-flow velocity for uniform jet velocity profile at the nozzle exit, the local flow velocity, u, and fuel concentration, Y_F, can be derived in terms of the non-dimensional axial distance, X, and radius, R, from the similarity solution in the following equations, respectively.

$$\frac{u-V_{co}}{u_0-V_{co}} = a\frac{\left(1-\frac{q}{a}\right)}{1-q}\frac{3}{32\left(X-X_v\right)}\frac{1}{\left[1+3a\left(1-\frac{q}{a}\right)\left(\frac{R}{32\left(X+X_v\right)}\right)^2\right]^2} \tag{4}$$

$$Y_F = a(2Sc+1)\frac{1}{32\left(X - X_{v,F}\right)}\frac{1}{\left[1+3a\left(1-\frac{q}{a}\right)\left(\frac{R}{32\left(X+X_{v,F}\right)}\right)^2\right]^{2Sc}}. \quad (5)$$

The non-dimensional axial distance and radius are defined as $X = x/(d\mathrm{Re})$ and $R = r/r_o$, respectively, where x is the distance from the fuel nozzle tip, r the radial distance from the centerline, d and r_0 the diameter and radius of the fuel nozzle, respectively, Re the Reynolds number defined as $u_0 d/v_\infty$, u_0 the initial jet velocity, and v_∞ the kinematic viscosity ($1.574\text{x}10^{-5}$ m^2/s was used, which is for 18% O_2 in 82% N_2). Also, V_{co} is the co-flow velocity, a the density ratio between the fuel and oxidizer ρ_F/ρ_∞, q the ratio between the co-flow velocity and initial jet velocity V_{co}/u_0, Sc the Schmidt number of C_3H_8 (Sc = 1.366) that was the fuel used in the experiments, and X_v and $X_{v,F}$ the virtual origins for velocity and concentration of the fuel jet, respectively.

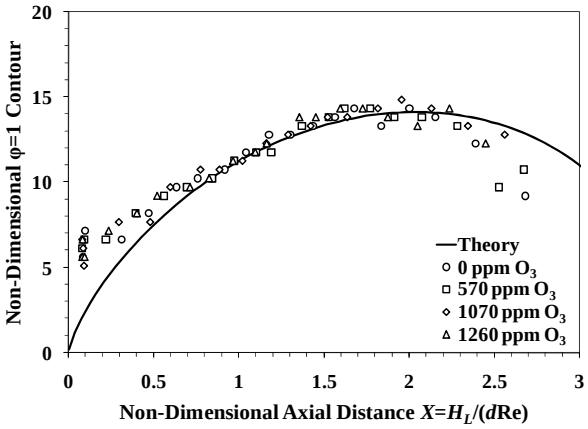

Fig.12 Plot of stoichiometric contour from the similarity solution and experimentally obtained flame radii.

Using the similarity equation for velocity and concentration, the stoichiometric contour was found and compared with the flame location in the experiments. **Figure 12** shows a plot of the experimental results of flame radius normalized by the nozzle radius at various conditions of fuel jet velocity with and without the presence of O_3 superimposed on a plot of the calculated cold flow stoichiometric contour. The good agreement between the flame radii with and without O_3 addition and the cold flow stoichiometric contour shows that the similarity solution of the flow is representative of the flame location. Furthermore, by assuming a thin flame and neglecting the effect of thermal expansion, the local flow velocities along the stoichiometric contour can be considered comparable to the lifted flame speed. The approximation of a thin reaction zone has been validated

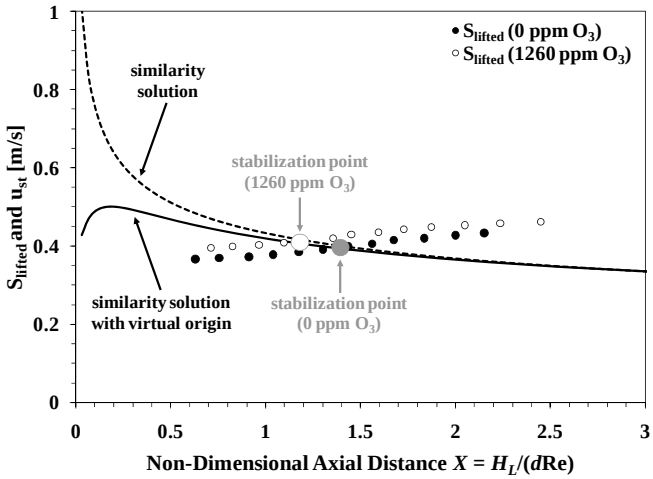

Fig. 13 Plot of the velocities along the stoichiometric contour found from similarity solutions with and without virtual origins along with the lifted flame speed with and without O_3 addition showing the flame stabilization mechanisms.

in previous experiments [53,54,55,56,57], by showing that the extrapolation of tribrachial flame speed to the zero mixture fraction gradient agrees well with the maximum propagation speed of tribrachial flames predicted theoretically.

To evaluate the enhancement with O_3 addition, an understanding of the flame stabilization mechanism is required. The stabilization mechanism of laminar lifted flames can be explained based upon the dynamic balance between the local flow velocity and flame speed along the stoichiometric contour. The leading edge of the lifted flame base at the premixed flame head always is located on the stoichiometric contour as shown in **Fig. 12**. The spatial profiles of local flow velocity from similarity solutions with and without the virtual origins are plotted in terms of non-dimensional axial distance, *X*, in **Fig. 13**. The flow velocities along the stoichiometric contour with and without the virtual origins are shown to deviate significantly when close to the fuel jet nozzle. Nevertheless, for the range of liftoff height used in the experiments, the deviation between the two solutions is on the order of 1%. Also plotted in **Fig. 13** are the lifted flame speeds with and without O_3 addition, which were converted from the measurements of lifted flame heights by varying the initial jet velocity. Normally, without O_3 addition, the lifted flame stabilizes where the local flow velocity on the stoichiometric contour is balanced with the lifted flame speed. When O_3 is added to the system, the flame propagation speed is enhanced, and the flame moves upstream to a new stabilization location where there is a dynamic balance. The result in **Fig. 13** indicates clearly that the lifted flame is stabilized by the balance between the local flow velocity and flame propagation speed with and without O_3 addition.

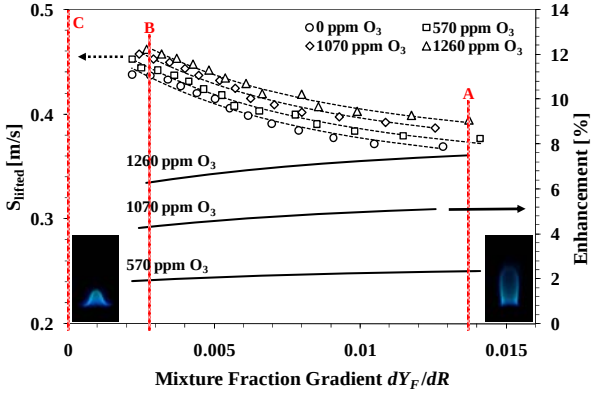

Fig. 14 Plot of the lifted flame speed, S_{lifted}, and percent enhancement of S_{lifted} as a function of mixture fraction gradient at 101.3 kPa with and without O_3 addition. The inset pictures of the lifted flames show the differences in the flame front near the fuel nozzle (right) and far from the fuel nozzle (left).

The lifted flame speeds were evaluated based upon the axial local flow velocity from the similarity solution of the cold flow at the measured liftoff heights with initial jet velocities. The results are plotted in **Fig. 14** as a function of fuel mixture fraction gradient. There is an enhancement of the lifted flame speed with increasing O_3 concentration. Interestingly, the enhancement of lifted flame speed increases with increasing fuel mixture fraction gradient for the same concentration of O_3. The observed enhancement can be explained reasonably with a coupling effect between kinetic enhancement and changes to the flame front curvature leading to a hydrodynamic enhancement by considering the unique characteristics of the triple flame structure of laminar lifted flames.

Firstly, numerical simulations were performed for equivalence ratios of 0.8 – 1.2 with and without 5000 ppm of O_3. This high concentration of O_3, which was larger than what was used in the experiments, was chosen in order to demonstrate more clearly what the effect was on the detailed structure of the flame that was not as easily observable numerically for lower O_3 concentrations. The results in **Fig. 15** show that the laminar flame speed is enhanced more for lean and rich equivalence ratios than at stoichiometric conditions. This result is reasonable because lean and rich premixed flames have relatively weaker reactivity and lower chemical heat release compared to the stoichiometric condition; therefore, the off-stoichiometric flame is more sensitive to the same amount of energy input associated with the addition of O_3. The lifted flame speed is also a strong function of the curvature at the premixed flame front that is coupled not only with the fuel mixture fraction gradient but also with the flow velocity gradient, hence hydrodynamics. The premixed flame curvature of the triple flame structure is determined by the change of laminar flame speed with the equivalence ratio and the upstream flow profile based on the dynamic balance between flame speed and local flow velocity. With O_3 addition to the co-flow of air, the non-uniform enhancement of laminar flame speed with the equivalence ratio induces an increase in the radius of the triple flame front since the lean and rich premixed flame will be enhanced more, as shown in **Fig. 15**. The larger radius of the flame leads to more significant flow redirection upstream of the flame; therefore, the local flow velocity at the premixed flame head will decrease and allow for enhanced lifted flame propagation speeds. Consequently, the lifted flame propagation speed is enhanced more by this effect because of the change in curvature of the flame front with O_3 addition.

Secondly, the increase of enhancement with larger mixture fraction gradient can be attributed to the change of velocity gradient in the radial direction when the liftoff height is decreased by the addition of O_3. Previous work demonstrated experimentally that the triple flame structure of the lifted flame is tilted by the velocity gradient change and the tilting angle is increased proportionally with an increase of the velocity gradient. Thus, when the lifted flame moves to an upstream position because of flame speed enhancement from the addition of O_3, the lifted flame front is subjected to a larger velocity gradient, tilting the flame front further. The effect of the velocity gradient becomes more significant when the lifted flame is at a location closer to the nozzle because the velocity gradient also non-linearly increases with the decrease of the lifted flame height from the fuel jet exit. Consequently, the current evaluation method of lifted flame speed may over-predict the enhancement of lifted flame speed since the axial local flow velocity has been considered only. The detailed effects on flame front geometry changes through tilting, curvature, and stretch are out of the scope of the current study; however, the flame front geometry changes are extremely

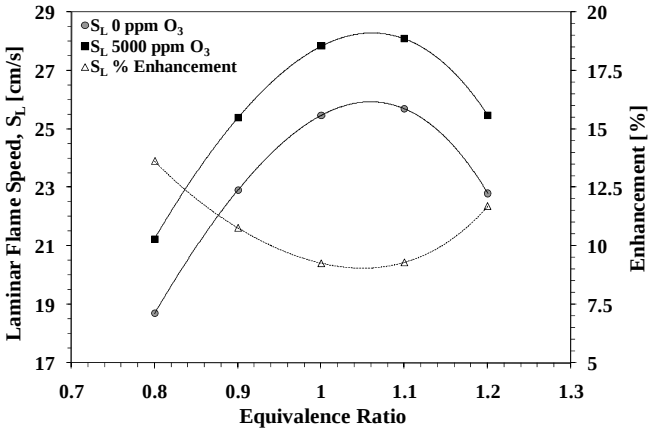

Fig. 15 Plot of the numerical simulation results of laminar flame speed, S_L, enhancement by O_3 as a function of equivalence ratio.

important because of the increased flame propagation enhancement beyond the purely kinetic effect. This effect has been termed the kinetic-induced hydrodynamic enhancement.

To exclude the complicated enhancement mechanism caused by the hydrodynamic effects discussed above and to focus on the kinetic enhancement of the lifted flame speed, the variation of the lifted flame speed with fuel mixture fraction gradient was extrapolated to a zero mixture fraction gradient. The process allowed for direct comparison with the stoichiometric laminar flame speed. In the limit of zero mixture fraction gradient and flame curvature, the lifted flame speed, S_{lifted}, is related to the laminar flame speed, S_L, through the unburned to burned density ratio [58]

$$S_{lifted} \approx S_L \sqrt{\frac{\rho_{unburned}}{\rho_{burned}}};$$

therefore, the experimental results of lifted flame speed could be compared to calculated laminar flame speeds.

The enhancement of the local lifted flame speed and the extrapolated lifted flame speed are plotted as a function of O_3 concentration in **Fig. 16** together with the numerical simulation results of purely kinetic enhancement. For the simulations with O_3 addition, the O atoms were conserved in order not to perturb the total oxidizer fraction in the mixture. Furthermore, the O_3 concentrations were adjusted to ppm concentrations for a stoichiometric flame instead of what was measured in the O_2 and N_2 mixture. For a large mixture fraction gradient, marked as *A* in **Fig. 14**, the enhancement is largest, as shown in **Fig. 16**. The factor-of-four difference in the flame speed enhancement between this fuel mixture fraction gradient and the purely kinetic enhancement are indicative of the kinetic-induced hydrodynamic enhancement described earlier in this section. For a small mixture fraction gradient, marked as *B* in **Fig. 14**, the local flame speed enhancement is lower, approaching the calculated purely kinetic enhancement results. The extrapolation to a zero mixture fraction gradient has been performed with a correlation factor $R > 0.99$ and agreed well with numerical simulation results, marked as *C* in **Fig. 14.** The deviation between experimental and numerical results becomes slightly larger for larger O_3 concentration. This effect once again is caused by the kinetic-induced hydrodynamic enhancement for larger concentrations of O_3. The smaller deviation between the extrapolated flame speed enhancement and the purely kinetic enhancement that was calculated is due to the extrapolation process averaging out the hydrodynamic enhancement. The details of the kinetic enhancement mechanism will be discussed in the following section with numerical simulation results.

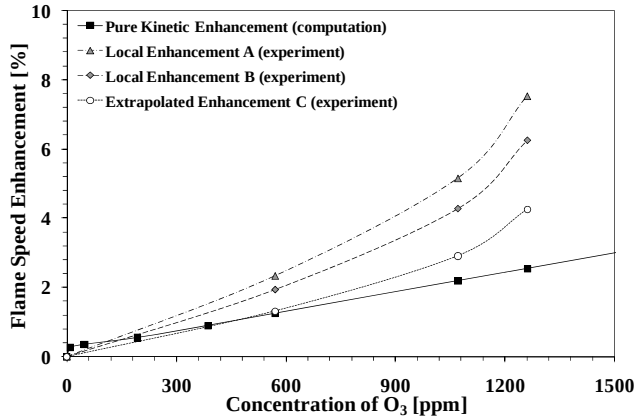

Fig. 16 Plot of experimental results compared to numerical simulations. The local enhancement of "A" and "B" are indicated for large and small mixture fraction gradients, respectively, shown in **Fig. 13**, while "C" indicates the lifted flame speed enhancement when extrapolated to a zero mixture fraction gradient.

To understand the flame speed enhancement pathways with O_3 addition, numerical simulations were performed using the PREMIX code from the CHEMKIN package [59]. The PREMIX code allows for one-dimensional calculations of laminar flames that can be used along with relation (5) to quantify the enhancement of lifted flame speed.

For the kinetic mechanism, the O_3 reactions [60,61] in **Table 2** were added to the C_3H_8 mechanism [62]. The two most important reactions were the decomposition reaction of

$$O_3 + M \leftrightarrow O_2 + O + M \tag{6}$$

and the O atom three body recombination reaction of

$$O + O + M \leftrightarrow O_2 + M \tag{7}$$

because of the production and consumption of O. The reaction of C_3H_8 with O_3 also was added but was not significant in the reaction system. The low impact of this reaction was because the reaction rate was several orders of magnitude slower than the O_3 decomposition reaction [63]. The reaction is slow because O_3 does not react rapidly with saturated hydrocarbons. The adapted mechanism allowed for accurate predictions of the laminar flame speed, temperature, and species profiles for C_3H_8 flames at a pressure of 101.3 kPa.

Reaction	**Reaction Constant [cm^3/mole/s]**	**Temperature Dependence**	**Activation Energy [kJ/mole]**
$O_3+O_2 \rightarrow O_2+O+O_2$	$1.54x10^{14}$	0	96.5
$O_3+O \rightarrow O_2+O+O$	$2.48x10^{15}$	0	95.09
$O_3+O_3 \rightarrow O_2+O+O_3$	$4.40x10^{14}$	0	96.5
$O_3+N_2 \rightarrow O_2+O+N_2$	$4.00x10^{14}$	0	94.84
$O_2+O+O_2 \rightarrow O_3+O_2$	$3.26x10^{19}$	-2.1	0
$O_2+O+N_2 \rightarrow O_3+N_2$	$1.60x10^{14}$	-0.4	-5.82
$O_2+O+O \rightarrow O_3+O$	$2.28x10^{15}$	-0.5	-5.82
$O_2+O+O_3 \rightarrow O_3+O_3$	$1.67x10^{15}$	-0.5	-5.82
$O_2+O_2 \rightarrow O+O+O_2$	$9.80x10^{24}$	-2.5	493.99
$O_2+O \rightarrow O+O+O$	$3.50x10^{25}$	-2.5	493.99
$O_2+O_3 \rightarrow O+O+O_3$	$1.20x10^{19}$	-1	493.99
$O_2+H_2O \rightarrow O+O+H_2O$	$1.20x10^{19}$	-1	493.99
$O+O+O_2 \rightarrow O_2+O_2$	$1.50x10^{16}$	-0.4	0
$O+O+N_2 \rightarrow O_2+N_2$	$6.00x10^{13}$	0	-7.49
$O+O+O \rightarrow O_2+O$	$5.34x10^{16}$	-0.4	0
$O+O+O_3 \rightarrow O_2+O_3$	$1.30x10^{14}$	0	-7.49
$O_2+O_2 \rightarrow O_3+O$	$1.20x10^{13}$	0	420.12
$O_3+O \rightarrow O_2+O_2$	$4.82x10^{12}$	0	17.14
$O_3+H \rightarrow O_2+OH$	$6.87x10^{13}$	0	3.64
$O_2+OH \rightarrow H+O_3$	$4.40x10^{7}$	1.4	329.44
$O_3+OH \rightarrow HO_2+O_2$	$9.60x10^{11}$	0	8.32
$O_3+HO_2 \rightarrow OH+O_2+O_2$	$1.66x10^{11}$	-0.3	8.32

Table 2 Rate constants for reactions of O_3 [60,61] that were added to the C_3H_8 chemical mechanism [62].

When the temperature, O, and O_3 concentration profiles were plotted, it became apparent that there was an increase in the temperature early in the pre-heat zone and a shifting of the overall temperature gradient (**Fig. 17**). The early pre-heat zone of the flame shows that a decrease in the O_3 concentration corresponds to an increase in the O concentration and the temperature profile.

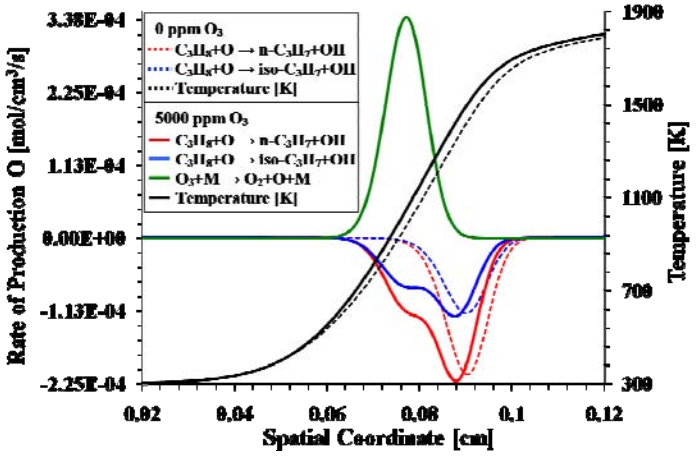

Fig. 17 Numerical simulation results showing the early rise in the temperature profile from chemical heat release and the rate of production of O with and without O_3 addition.

A rate of production analysis was performed to understand the underlying flux of species and the overall enhancement mechanism. In **Fig. 17**, the rate of production of O shows that, upon O_3 decomposition because of the slightly elevated temperatures in the pre-heat zone, O rapidly reacts with the fuel via the reactions

$$C_3H_8 + O \rightarrow n - C_3H_7 + OH \quad (8)$$

$$C_3H_8 + O \rightarrow iso - C_3H_7 + OH \quad (9)$$

Reactions (8) and (9) provide the first key initiation steps in the extraction of chemical heat release by abstracting an H atom from the parent fuel to produce OH. Simultaneously, OH also is produced from the reaction of O_3 with H via

$$O_3 + H \rightarrow OH + O_2\,, \quad (10)$$

shown in **Fig. 18**. The rate constant for this reaction is given in **Table 2**. Reactions (8) – (10) are important because they provide the OH necessary to react and form H_2O and thermal energy release to enhance the flame speed. A rate of production of OH analysis is shown in **Fig. 18** and identifies the major reaction pathways that change significantly in the early stages of the flame following O_3 decomposition. The three most important reactions are

$$CH_2O + OH \rightarrow HCO + H_2O \quad (11)$$

$$OH + HO_2 \rightarrow H_2O + O_2 \quad (12)$$

$$C_3H_8 + OH \rightarrow iso - C_3H_7 + H_2O\,. \quad (13)$$

While reactions (11) – (13) all form H_2O to produce heat release early in the flame, the two most important reactions are (11) and (12). The rate of heat release early in the pre-heat zone of the flame shows that reactions (11) and (12) are significant contributors of thermal energy, which elevates the temperature. **Figure 19** shows increased chemical heat release at lower temperatures with O_3 addition, with the most significant impact between 700 K and 1300 K. The elevated levels of heat release earlier in the flame accelerate other reactions to change the structure of the flame, which, in turn, enhance the rate at which the flame can propagate. Furthermore, **Fig. 19** shows that the peak heat release is higher with O_3 addition because of the additional energy that was coupled into the system by the plasma.

The enhancement scheme begins with the decomposition of O_3 by reaction (6) early in the pre-heat zone of the flame, releasing O that rapidly reacts with the parent fuel via reactions (8) and (9). The OH that is produced then reacts to form H_2O and heat mostly via reactions (11) and (12) to elevate the temperatures. The elevated temperatures promote more rapid reactions early in the flame to enhance the flame propagation speed. The O_3 acts as a transporter of energy from the plasma to the early stages of the flame in the pre-heat zone, where it seeds O into the flow to extract chemical heat release.

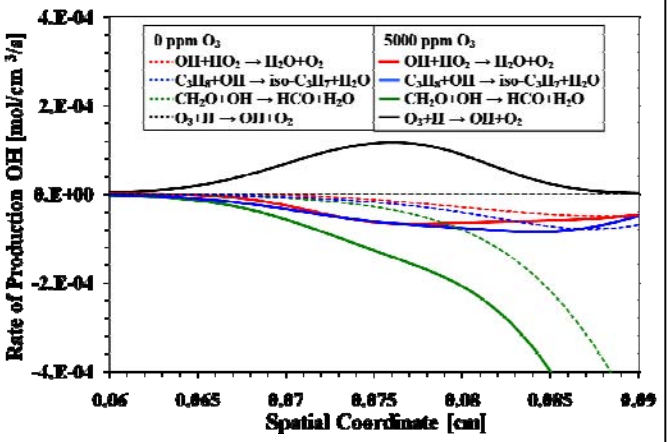

Fig.18 Fig. 11 Rate of production of OH showing change of reaction pathways with O_3 addition to create stable products and heat release for flame speed enhancement.

To demonstrate that the effect was not just simply the heat released after the decomposition of O_3 and recombination of O, a fictitious reaction was added to the mechanism to quench the O_3 to O_2 to extract all of the energy to the flow far upstream of the flame zone. This comparison was accomplished by adding the reaction of

$$O_3 + O_3 \rightarrow O_2 + O_2 + O_2 \qquad (14)$$

with a rate sufficiently fast to consume all of the O_3 far upstream of the flame front, where the temperature was 300 K. The results of the flame speed enhancement with and without reaction (14) are shown in **Fig. 20** along with the experimental data. It is shown clearly that when O_3 quenches far upstream of the flame, the temperature only increases by several degrees to enhance the flame speed much less than when O_3 reaches the flame pre-heat zone; therefore, when O_3 reaches the pre-heat zone of the flame, some chemical heat release is extracted to give significant flame speed enhancement. Furthermore, the results in **Fig. 20** also show good agreement between the enhancements found in the experiments and in the computations when the O_3 reaches the pre-heat zone of the flame.

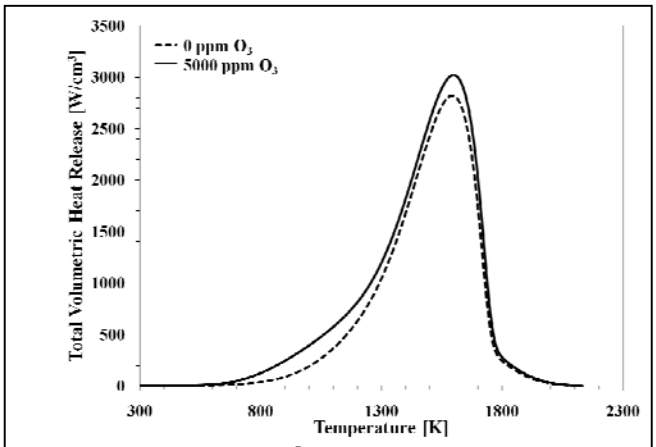

Fig. 19 Heat release versus temperature showing elevated levels of chemical heat release at lower temperatures with O_3 addition.

With the knowledge that O_3 addition to a lifted flame will enhance flame propagation speed significantly, it is of interest to take into account the efficiency of producing O_3. If one considers the production of O_3 in a dielectric barrier, which is the most common production method, there exists a critical concentration at which the maximum flame speed enhancement is achieved. If large amounts of power are supplied to the discharge to produce high concentrations of O, the recombination of O to O_2 becomes a significant pathway, competing with the O_3 production pathway of reaction (6). For example, if a concentration of 1% O is produced, every second O atom recombines to O_2 instead of forming O_3. On the other hand, if the power of the discharge is too low, the energy loss to ions becomes increasingly important. A reasonable compromise is found when the dissociation in the plasma discharge reaches approximately 0.2%; therefore, with 0.2% (2000 ppm) of O_3, the kinetic enhancement of flame speed would be approximately 4%. With the addition of the changes in the flame front curvature caused by the kinetic enhancement, the overall flame speed would be enhanced between 10% and 15%; therefore, in a practical system, the production and injection of O_3 in the cold transport to a flame can yield significant flame propagation enhancement with minimal energy expenditure.

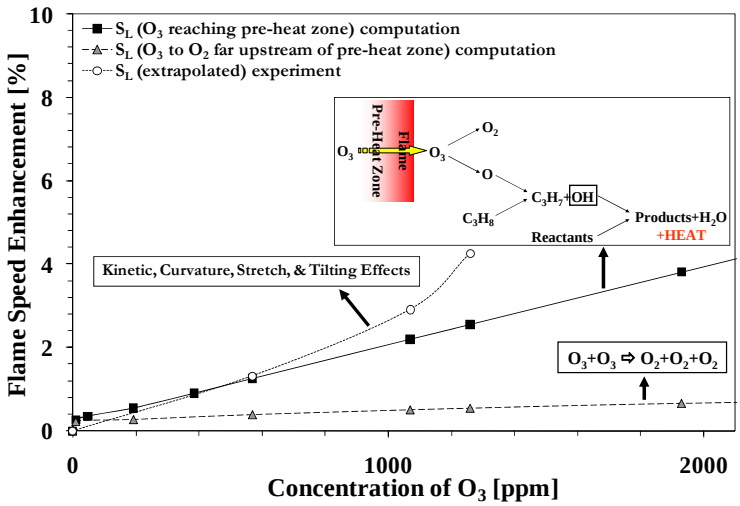

Fig. 20 Comparison plot of experimental results and numerical simulation results showing kinetic enhancement by O_3.

2.2.4. Conclusions

A platform to study quantitatively the enhancement effects of plasma-produced O_3 on hydrocarbon flame speeds was developed. O_3 had significant kinetic enhancement effects on the propagation speeds of C_3H_8 lifted flames. Plasma-produced O_3 becomes a carrier of O at low temperatures. Since the lifetime of O is extremely short, especially at room temperature because of recombination and wall quenching reactions, the attachment of O to O_2 allows for extended cold transport of O. With temperatures lower than approximately 400 K, the O_3 can transport O atoms almost indefinitely to a reaction system. The only difference in enhancement will come from the energy required to break the bond of the weakly attached O in O_3, which requires much less energy than producing O from O_2. Numerical simulation results showed that the O released upon O_3 decomposition in the preheating- zone of the flame reacted rapidly with the fuel and atomic H to produce OH, which subsequently reacted with fuel and fuel fragments such as CH_2O to form H_2O and accelerated fuel oxidation. The chemical heat release early in the preheating zone of the flame resulted in increased propagation speed of the flame.

Equally important was the coupling effect that the kinetic enhancement had on the hydrodynamics at the flame front. The fuel and velocity gradients at the premixed flame head

create a unique triple flame front with curvature, stretch, and tilting relative to the flow. Because of the unique triple flame structure of lifted flames, the presence of O_3 at the flame front creates a kinetic enhancement that also induces hydrodynamic enhancement. The maximum overall flame speed enhancement in the laboratory coordinate was shown to be as high as 8% with 1260 ppm of O_3, while the enhancement locally was much lower at about 3%. When extrapolated to a zero mixture fraction gradient where the hydrodynamics of the flame were averaged and minimized, the enhancement was comparable to the pure kinetic enhancement at approximately 4%. The results indicate the very important finding that, in a practical system where there are fuel and velocity gradients, stretch, curvature, tilting, and significant concentrations of O_3, the flame speed can be enhanced greatly.

The results of the current research imply that, when energy is coupled into specific plasma-produced species, there is no requirement for the control of heat loss. For example, if energy is coupled into a reactive flow to raise the translational gas temperature only, there needs to be careful thermal management. When energy is coupled into stable species, no thermal management needs to be considered for O_3 when the temperatures are below approximately 400 K. The energy contained within the species can be transported for significant distances and residence times and extracted at the combustion reaction zone.

Ozone addition illustrates the importance of timescales because, if O_3 decomposes far upstream of the flame, the O released would recombine and not react with the fuel because the temperatures would not be high enough to support the propagation of those reactions within the flow residence time to the flame, but when the O_3 decomposes and releases O to the reactants when the temperatures were only slightly elevated above the ambient, the fuel-plus-O reactions became dominant over recombination and quenching reactions. The chemical enthalpy that was extracted upstream of the flame stimulates other reactions, as well as the diffusion of heat, enhancing the propagation of the flame; therefore, the competition between the time scales of collisional quenching and reactive quenching is extremely critical when trying to achieve combustion enhancement through plasma activation.

Lastly, this work demonstrated another important step in developing an understanding of the most important plasma-produced species. With the knowledge of NO_x and O_3, less stable and shorter lifetime plasma-produced species now can be investigated more thoroughly. The results of O_3 enhancement of flame propagation speed provided here gives a firm foundation, since O_3 always will exist in an oxygen-containing plasma; therefore, the pursuit of shorter lifetime excited oxygen species, such as $O_2(a^1\Delta_g)$, can be pursued. The results of the effects of $O_2(a^1\Delta_g)$ on flame propagation speed using a lifted flame apparatus at reduced pressures are discussed in the next section.

2.3 Flame Propagation Enhancement by Plasma Generated $O_2(a^1\Delta_g)$

2.3.1Experimental System

A laminar lifted flame burner in **Fig.21** was adopted for the combustion platform and was placed in a variable pressure chamber that could be used from atmospheric pressure down to 2.67 kPa with the installed vacuum and flow system. The lifted flame burner consisted of a central fuel jet with a diameter of 1.04 mm and was located in a 90 mm inner diameter fused silica (quartz) tube to contain the co-flow of O_2 and Ar in the chamber. The gases used in the experiments were C_2H_4 for the fuel and ultra-high purity O_2 (99.99%) and Ar (99.95%) mixed for the oxidizer. The flow rate of the fuel was controlled with a calibrated mass flow meter,

while the O_2 and Ar were controlled with calibrated sonic nozzles to give flow rate uncertainties of less than 1%.

To excite the co-flow in the low pressure experiments, an electrodeless microwave discharge (McCarroll cavity driven by an Opthos MPG-4M microwave power supply) with up to 100 Watts of power was used external to the chamber upstream of the lifted flame burner to activate the O_2 in the mainly Ar flow (15% O_2 in 85% Ar for 3.61 kPa and 11.9% O_2 in 88.1% Ar for 6.73 kPa). The plasma was initiated in the microwave cavity by seeding the upstream flow with ionized gas created by a high-voltage, high-frequency Tesla coil. The mixture of ultra-high purity O_2/Ar was activated by the self-sustained microwave discharge that was maintained when the Tesla coil was switched off. The plasma system was chosen because of its flexibility of being used external to a quartz tube flow system, as well as its ease of tuning and stability for the range of pressures used in the experiments. Furthermore, the lower power output of the plasma system produced a glow discharge with a lower reduced electric field and an electron energy distribution function that was peaked at lower electron temperature where significant concentrations of $O_2(a^1\Delta_g)$ could be excited from ground state O_2. Nevertheless, the microwave discharge produced excited Ar, as well as multiple oxygen-containing species, including O, O_3, $O_2(v)$, $O(^1D)$, $O(^1S)$, $O_2(a^1\Delta_g)$, $O_2(b^1\Sigma_g)$, etc.

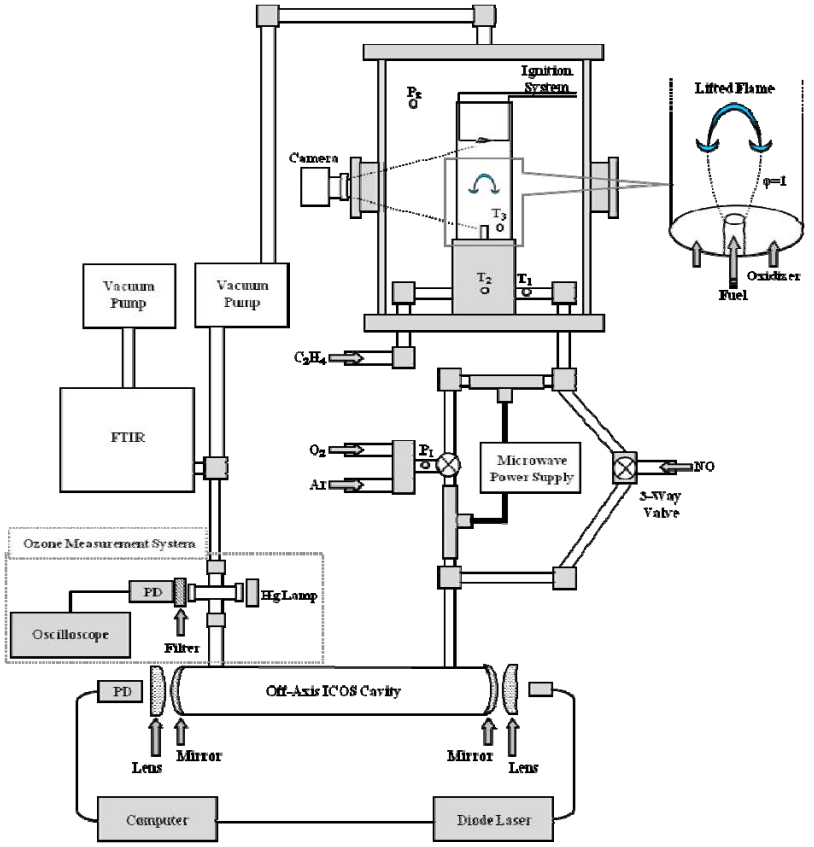

Fig. 21 Experimental set-up schematic of variable pressure lifted flame burner integrated with microwave plasma discharge device and plasma flow diagnostics system. The abbreviation "PD" denotes photodetector.

The high-velocity fuel jet (approximately 20 m/s – 40 m/s) and low-velocity co-flow (approximately 0.15 m/s – 0.2 m/s) created a mixing layer with a stoichiometric contour where the premixed flame head of a lifted flame was located (shown in the top right insert in **Fig. 21**). The lifted flame, which is also called a tribrachial (triple) flame, had a premixed flame head and diffusion flame tail where the flame always was anchored on the stoichiometric contour. The lifted flame could be located at different distances from the fuel jet nozzle depending upon the local flow velocity. For a fixed flow field, the flame was located in a stationary position, where the lifted flame speed at

the premixed flame head was balanced with the local flow velocity. If the flame speed increased, the liftoff height decreased to re-establish a local dynamic balance between the flame speed and flow velocity.

Due to the slow laminar boundary layer development and the velocity and concentration gradients created, the lifted flame height was very sensitive to the changes in flame speed and therefore provided excellent flame geometry for the direct observation of flame speed enhancement. Since the fuel and oxidizer were not mixed far upstream of the flame, there was very short residence time for the fuel and oxidizer to react in the cold flow. The short residence time helped to decouple the enhancement effects further to be directly from reactions in the flame zone and not far upstream in the cold unreacted flow.

All surfaces with which the plasma afterglow gases came in contact were treated as chemically inert. The tubing used was fused silica (quartz), the fittings were 316 stainless steel (non-magnetic), and the lifted flame burner was coated with silica (Restek Silcosteel). The inert surfaces mitigated the quenching from active wall surfaces and promoted the transport of $O_2(a^1\Delta_g)$ to the flame. Multiple temperatures and pressures were monitored and recorded in the system with thermocouples and pressure transducers, respectively. Temperatures were measured at points T_1, T_2, and T_3 shown in **Fig. 21**, corresponding to the burner inlet tube surface temperature, burner surface temperature, and co-flow gas temperature. Additionally, the pressure upstream of the microwave plasma and in the chamber, respectively at points P_1 and P_2 in **Fig. 21**, were monitored continuously and recorded.

The plasma-activated oxidizer flow was run through a series of diagnostics to quantify the concentrations of species produced by the plasma. The flow system used the same chemically inert flow surfaces and residence times for a direct comparison to the lifted flame system. The diagnostics were not run in situ with the flame system but instead as two separate systems with common flow control and plasma discharge. The systems were used separately because having the ICOS cavity between the plasma and flame would double the transport residence time and decrease the concentrations of the species of interest. For the 3.61 kPa and 6.73 kPa experiments, the residence times from the plasma to the end of the ICOS cavity were approximately 1320 milliseconds and 1680 milliseconds, respectively, and between the plasma and flame in the burner the times were approximately 910 milliseconds and 1470 milliseconds, respectively.

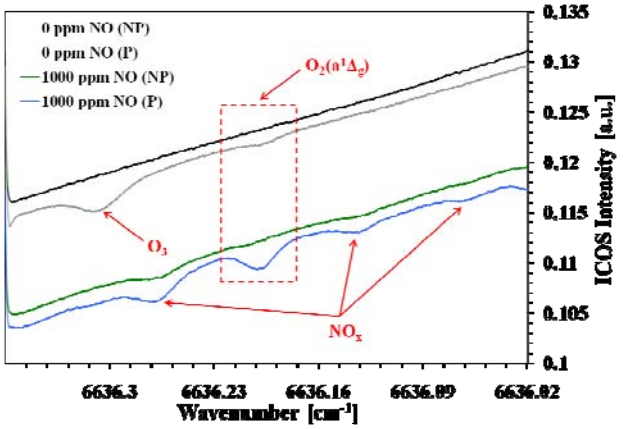

Fig.22 ICOS transmittance spectrum with and without NO addition and plasma activation (P and NP are plasma and no plasma, respectively).

The $O_2(a^1\Delta_g)$ produced by the microwave plasma discharge was measured by using highly sensitive integrated-cavity-output spectroscopy by absorption at the (1,0) band of the $b^1\Sigma_g^+ - a^1\Delta_g$ Noxon system [64]. The ICOS system measured the average number density of $O_2(a^1\Delta_g)$ across an 82.5 cm long (approximately 1500 millisecond residence time) absorption cell downstream of the plasma. The effective path length was greater than 78 kilometers due to multiple passes and

provided accurate measurements down to 10^{14} molecules/cm^3. In **Fig. 22** the transmittance spectra from the ICOS cavity for the experimental conditions with and without NO addition and plasma activation are shown. The absorption feature demarcated by the red box shows the location of the Q(12) transition of $O_2(a^1\Delta_g)$, which was the primary transition of interest [64]. The Q(12) transition was chosen for absorption measurements because there was no interference between it and any of the absorption features of other species present in the flow. In **Fig. 23** the measured absorption profile of $O_2(a^1\Delta_g)$ using the Q(12) transition for plasma-activated Ar/O_2 at 3.61 kPa is shown. The fitted curve in **Fig. 23** was a function of the absorption pathlength and cross section, as well as broadening from pressure and temperature. A more detailed description of the measurement and curve fitting process to obtain absolute number densities of $O_2(a^1\Delta_g)$ can be found in previous work [64].

The isolation of $O_2(a^1\Delta_g)$ in the plasma afterglow was achieved with the addition of a small concentration of NO to the flow. The details of this approach are described in previous section. Quantitative measurements of NO and NO_2 were required to confirm the presence of these species in the system. To accomplish these measurements the flow was split downstream of the O_3 absorption cell to allow sampling with Fourier transform infrared (FTIR) spectroscopy. The pressure and temperature were fixed at 2 kPa and 373 K, respectively, in the FTIR cell for all experimental measurements to maintain sufficient flow rates and sampling times. The absorption features of NO and NO_2 were chosen where there would be no chance of interference from changes in the background or other species.

To avoid the complications of plasma disturbances in the combustion system, the flow was activated far upstream of the lifted flame. With the flow rates used in the experiments, the average residence times between the plasma and the flame were approximately one second. The significantly long residence time was chosen in order to quench the plasma-produced species that were not of interest in the experiments. Since the focus of the current experiments was to isolate $O_2(a^1\Delta_g)$, Ar was used as the inert instead of N_2. Using Ar served two purposes. First, Ar has only electronic excitation requiring 11.6 eV for the first electronic level; therefore, when using the low-power microwave system, most of the energy then will be deposited into the O_2 to produce O, O_3, $O_2(a^1\Delta_g)$, $O_2(b^1\Sigma_g)$, and metastable O and Ar. Second, without N_2, there would be no nitrogen-containing species produced, specifically NO or NO_2, simplifying the chemistry in the plasma and in the post-plasma flow.

With the one second residence time, the only two species that have long enough lifetime to allow for measurement and introduction to a combustion system are O_3 and $O_2(a^1\Delta_g)$. A list of the primary quenching reactions of the oxygen containing species is given in **Table 3** in order of decreasing reaction rate. Quenching reactions with O_2 dominate over the inert species present and are, therefore, the reactions listed for a comparison. Ozone is the most stable species, with $O_2(a^1\Delta_g)$ also having a long lifetime. All other species are quenched many times faster.

Beyond the gas-phase kinetics, the wall quenching effects have to be considered. Many species can be transported significant distances with inert wall surfaces; therefore, coating all wall surfaces with quartz or using quartz tubes is essential to ensure minimal quenching. Some examples of the relative reaction probabilities of plasma-produced species with a wall surface of Pyrex (similar to quartz) are shown in **Table 4**. Having large surface to volume ratios in the flow will suppress the concentrations of all species except O_3 and $O_2(a^1\Delta_g)$.

Reaction	Reaction Constant [cm^3/molecule/s]
$O+O_2+M \rightarrow O_3+M$	$6.0x10^{-34}$ = (HP limit $3.61x10^{-10}$)
$O(^1D)+O_2 \rightarrow O+O_2$	$4.0x10^{-11}$
$O_2(v)+O_2 \rightarrow O_2+O_2$	$1.73x10^{-13}$
$O_2(b^1\Sigma_g)+O_2 \rightarrow O_2+O_2$	$4.1x10^{-17}$
$O_2(a^1\Delta_g)+O_2 \rightarrow O_2+O_2$	$1.6x10^{-18}$
$O_2(a^1\Delta_g)+Ar \rightarrow O_2+Ar$	$1.0x10^{-20}$

Table 3 Reaction rates of plasma-produced oxygen species at 298 K. The term "HP" refers to the high pressure limit.

Wall Reaction	Reaction Probability
$O_2(a^1\Delta_g)+wall \rightarrow O_2$	$2x10^{-5}$
$O_2(b^1\Sigma_g)+wall \rightarrow O_2$	$2x10^{-2}$
$O_2(v)+wall \rightarrow O_2$	0.2
$O(^1D)+wall \rightarrow O(^3P)$	1.0
$O(^1S)+wall \rightarrow O(^3P)$	1.0
$O+wall \rightarrow ½O_2$	$2x10^{-2}$
$M^+ +wall \rightarrow M$	1.0

Table 4 Wall quenching probabilities of plasma-produced species for a Pyrex surface.

There remained the need to isolate O_3 and $O_2(a^1\Delta_g)$ to observe their individual effects. Ozone can be isolated by simply using higher pressures because the $O_2(a^1\Delta_g)$ will be quenched collisionally to $O_2(X^3\Sigma_g)$. To isolate $O_2(a^1\Delta_g)$, a different approach needs to be taken to remove O_3. To mitigate the effect of O_3 and completely isolate the effect of $O_2(a^1\Delta_g)$, NO was added to the flow downstream of the plasma in the flow diagnostics system, as well as the combustion system. The addition of NO in prescribed concentrations served two purposes. First, it catalytically removed O_3 from the system to isolate $O_2(a^1\Delta_g)$, and second, NO addition in the concentrations in the experiments would not interfere with the effects of $O_2(a^1\Delta_g)$.

The isolation of $O_2(a^1\Delta_g)$ with NO addition relies upon the reaction of NO with O_3 via

$$NO + O_3 \rightarrow NO_2 + O_2 . \quad (15)$$

Reaction (15) is over three-orders of magnitude faster than NO with $O_2(a^1\Delta_g)$, as shown in **Table 5**. The subsequent reaction of NO_2 with $O_2(a^1\Delta_g)$ is also slow in comparison to reaction (15). The major consumption pathway of NO_2 would be from the reaction with O atoms via

$$NO_2 + O \rightarrow NO + O_2 . \quad (16)$$

Since O and O_3 are present at the same location in the flow tube, i.e., O atoms are converted to O_3, NO acts as a catalyst, and very little is needed to eliminate the O_3 fully. The individual effects of $O_2(a^1\Delta_g)$ can be selected by the use of NO addition. Finally, the presence of NO also can be used to determine the presence of O atoms via the well known O atom titration reaction

$$NO + O \rightarrow NO_2^* \rightarrow NO_2 + h\nu . \quad (17)$$

The absence of the greenish-yellow color in the plasma afterglow is used to assure that all the O atoms are quenched and not present in the flow system.

Reaction	Reaction Constant (cm^3/molecule/s)
$O_2(a^1\Delta_g)+NO \rightarrow O_2+NO$	$4.48x10^{-17}$ [45]
$O_2(a^1\Delta_g)+NO \rightarrow O+NO_2$	$4.88x10^{-18}$ [42]
$O_2(a^1\Delta_g)+NO_2 \rightarrow O_2+NO_2$	$5.00x10^{-18}$ [42]
$O_3+NO \rightarrow O_2+NO_2$	$1.80x10^{-14}$ [40]
$O_3+NO_2 \rightarrow O_2+O_2+NO$	$1.00x10^{-18}$ [46]

Table 5 Reaction rates of $O_2(a^1\Delta_g)$ and O_3 with NO and NO_2 at 298 K.

2.3.2 Results and Discussion

To investigate the flame speed enhancement by $O_2(a^1\Delta_g)$, reduced pressures were used to suppress the quenching and recombination rates. The ICOS and O_3 absorption diagnostics were used initially to measure $O_2(a^1\Delta_g)$ and O_3 as functions of pressure and O_2 concentrations. The results in **Fig. 23** show that there remain significant concentrations of O_3, despite the decrease of the pressure. At lower pressure and O_2 loading in Ar, the $O_2(a^1\Delta_g)$ was in significantly greater concentration than O_3. Unfortunately, stable flames under lower pressure and O_2 loadings were difficult to achieve; therefore, the removal of O_3 was warranted for the isolated study of $O_2(a^1\Delta_g)$.

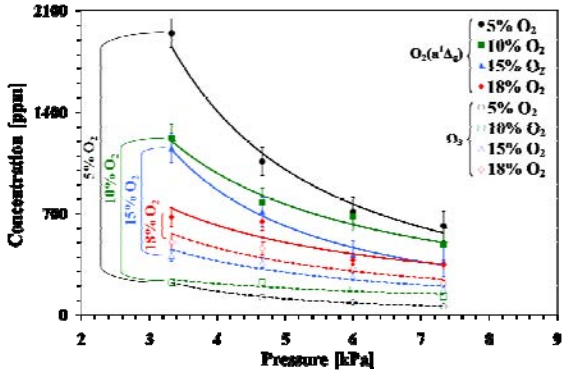

Fig.23 Experimentally measured concentrations of O_3 and $O_2(a^1\Delta_g)$ as a function of pressure before O_3 reduction by NO addition.

The results in **Fig. 24** show that the addition of NO suppressed the concentration of O_3 below the threshold that could be measured (ppm levels), while the $O_2(a^1\Delta_g)$ concentration at a given residence time increased by almost an order of magnitude over a wide pressure range. Since the NO addition worked catalytically to reduce the $O_2(a^1\Delta_g)$-quenching species of O_3 and O through reactions (15) and (16), the process was heavily reliant upon the concentration of O where the NO was added to the system. With the flow rates used in the system, the residence time between the plasma and the location of NO addition was approximately 5 ms. For the pressures used in the experiments, there was a significant concentration of O in relation to O_3; nevertheless, the concentrations of NO and NO_2 needed to be verified to ensure that the NO_2 concentration remained negligible.

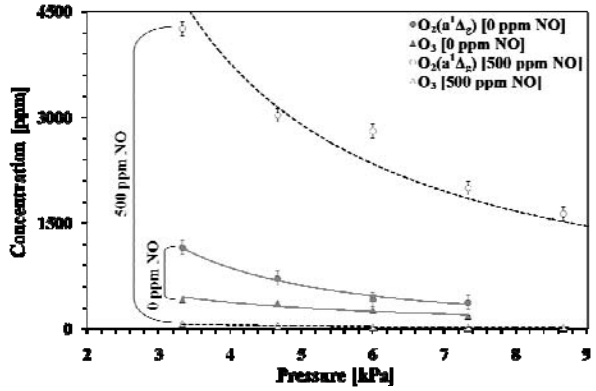

Fig.24 Experimentally measured concentrations of $O_2(a^1\Delta_g)$ and O_3 with and without 500 ppm NO for 15% O_2 in 85% Ar as a function of pressure.

To confirm that there was no conversion of NO to NO_2, measurements were taken using the FTIR with the plasma off and on. The measurements were taken initially of the plasma off, where the FTIR measured the exact concentration of NO that was being added to the system. When the plasma was turned on, the NO concentration did not change, as shown in **Fig. 25**. To confirm further that there was no NO_2 production, **Fig. 26** shows that the concentration of NO_2 remained below the detectability threshold of the FTIR. Two reference absorption spectra of 500 ppm and 4000 ppm NO_2 that were taken at the same pressures and temperatures are shown for comparison and to demonstrate that that the three peaks present can be resolved. The results show clearly that the highest concentration of NO_2 was on the order of 10's of ppm. Since flame speed enhancement by NO_2 is more than a factor of three smaller than the effect of O_3 for the same concentrations, the small concentration of NO_2 would have a negligible effect on flame speed. When NO was added to the plasma afterglow, the only plasma-produced species to survive would be $O_2(a^1\Delta_g)$, and the NO concentration would remain constant.

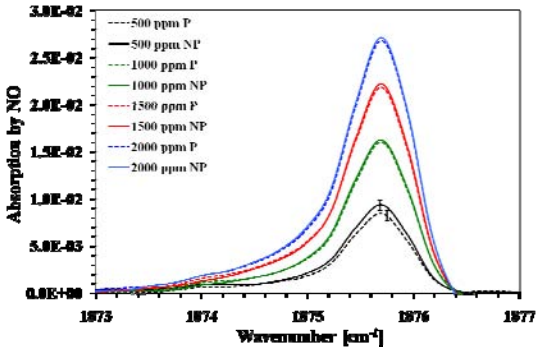

Fig.25 NO absorption measurements from FTIR showing that the NO concentrations did not change with the plasma on or off and therefore no conversion to NO_2 (P and NP are plasma and no plasma, respectively).

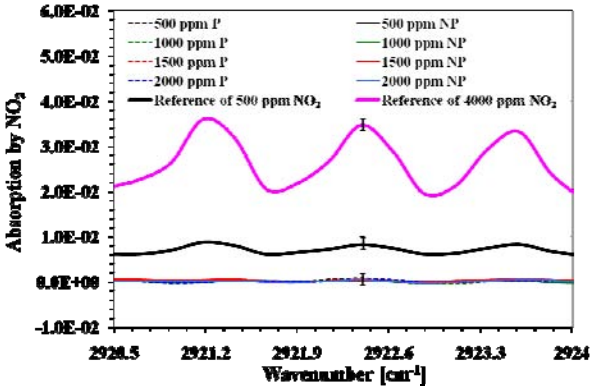

Fig. 26 NO_2 absorption measurements from FTIR showing that the NO is not converted to NO_2 when the plasma is on or off (P and NP are plasma and no plasma, respectively).

To confirm further the chemical kinetic processes involved in the post-discharge gases in the system, a simple flow kinetic model was compiled to include O, O_3, $O_2(a^1\Delta_g)$, N_2, and Ar. Nitrogen was included in the model because the NO being injected into the system downstream of the plasma was accompanied by N_2. The presence of N_2 did not affect any of the results because N_2 did not react with any of the other species present in the system. The most critical reaction would be with $O_2(a^1\Delta_g)$, but the quenching rate is of the same order as the rate with Ar. One of the most important initial conditions for the numerical simulations was the concentration of atomic oxygen. To find what concentrations existed in the experiments, an NO_2 titration technique was adopted. NO_2 was added to the plasma afterglow at the same location of NO injection, approximately 5 ms downstream of the plasma. The NO_2 titration technique works by reaction (16) being five orders of magnitude faster than reaction (17); therefore, when NO_2 was injected after the plasma, the FTIR was used to sample the flow downstream and monitor the NO-versus-NO_2 concentration. The NO_2 was added continually until the FTIR showed the presence of NO_2 and no changes in

the concentration of NO. At that point, the concentration of NO_2 being added was equal to the concentration of O at the injection location in the flow. Furthermore, the lack of emission from reaction (17) also would indicate that O was no longer present in the flow. The NO_2 titration technique provided quantification of the O concentration within a 10% uncertainty to be used as an initial condition in the kinetic model.

Without NO addition to the plasma afterglow, the model predicted the concentrations of O_3 and $O_2(a^1\Delta_g)$ well. With NO addition, if the simple flow kinetic model was maintained at 300 K, the catalytic cycle to remove O_3 was not complete and produced significant concentrations of NO_2. Reaction (16) was not participating, possibly from the lack of presence of O. Realizing that the temperature of the gas in the plasma afterglow is not 300 K but starts at a temperature around 450 K and decreases to nearly room temperature after a short residence time, the model was adjusted to account for this temperature condition. With a prescribed temperature gradient, the results with NO addition showed clearly that the catalytic cycle did not consume any NO and the NO_2 remained negligible (**Fig. 27**). Furthermore, the results without NO addition agreed well with the experiments (**Fig. 27**). The temperature gradient was critical to the catalytic cycle because of the quenching reactions of atomic oxygen. When the temperature was fixed at 300 K, the O atoms quenched quickly to produce O_3, therefore not allowing the NO_2 to be converted back to NO. When the temperatures were higher at the beginning of the computation, the recombination reactions were suppressed, allowing for the catalytic cycle to be completed.

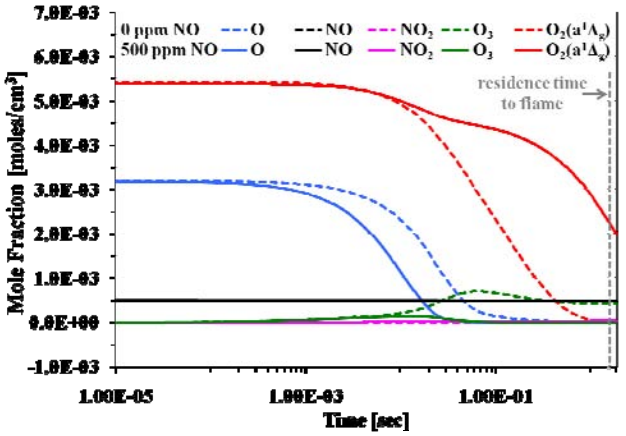

Fig.27 Plot of numerical simulation results of plasma afterglow species profiles with and without NO addition.

The validation of the simple flow model with the experimental results allowed for it to be used to find the concentrations of $O_2(a^1\Delta_g)$ at the residence time of the flame in the burner system. The change of $O_2(a^1\Delta_g)$ concentration at the residence time of the flame was very small, allowing for minimal error; therefore, the $O_2(a^1\Delta_g)$ could be measured in the ICOS cavity and the kinetic model used to find the actual concentration at the specific flow residence time of the flame in the combustion system.

To examine the effects of $O_2(a^1\Delta_g)$ on flame propagation speed, C_2H_4 was used as the fuel to produce stable lifted flames at low pressures. The co-flow conditions of velocity and O_2 concentration in Ar were fixed, along with the fuel jet velocity, to establish a flame at a stationary lifted location. Photographs were taken of the flame while simultaneously recording the pressure and temperature. The microwave plasma then was turned on and photographs taken again of the flame with a lower liftoff height. The change in flame liftoff height was calculated from the photographs. A similar procedure was used again with NO addition just downstream of the microwave plasma cavity, replicating the residence times in the plasma afterglow diagnostics system. The results showed that there was a significant change in the flame liftoff height when the plasma was turned on with and without the addition of NO; therefore, the flame propagation enhancement came from a combination of O_3 and $O_2(a^1\Delta_g)$ without NO addition and only from

$O_2(a^1\Delta_g)$ with NO addition. Concentrations between 500 ppm and 2000 ppm of NO were added downstream of the plasma to give different concentrations of $O_2(a^1\Delta_g)$ at the flame front. The more NO that was added, the faster the O_3 and O were quenched before they quenched $O_2(a^1\Delta_g)$.

The experiments were performed for several conditions at both 3.61 kPa and 6.73 kPa. The flow field, temperature, and pressure remained constant when the plasma was cycled off and on, so a direct comparison between plasma off and on conditions can be attributed to the enhancement by O_3 and $O_2(a^1\Delta_g)$. The temperature and pressure remained constant within an uncertainty of 0.1 K and 26.7 Pa respectively. Experiments were performed to verify quantitatively that the uncertainty in temperature and pressure was not affecting the flame liftoff height enough to mask the enhancement by O_3 and $O_2(a^1\Delta_g)$ addition. For a temperature change of 0.1 K, the flame liftoff height changed by 0.07 mm, and for a pressure change of 26.7 Pa the flame liftoff height changed by 0.29 mm. For the change in flame liftoff height observed in the experiments with O_3 and $O_2(a^1\Delta_g)$ addition, which was on the order of 5 mm to 10 mm, the uncertainty was more than an order of magnitude smaller.

The presence of NO did affect the flame structure by changing the stoichiometric contour and flame speed slightly, but the comparison was between the plasma being off and on with constant NO addition. Since the flow diagnostics showed that the NO acted catalytically to reduce the O_3 and did not change in concentration, the conditions of the plasma being off and on could be compared directly. The near-zero concentrations of NO_2 would have a negligible effect on flame speed, since the enhancement was calculated to be more than three times lower than that of O_3.

$O_2(a^1\Delta_g)$ [ppm]	**O_3 [ppm]**	**ΔH_L [mm]**
215	513	7.15
3851	0	4.76
5416	0	7.31
5571	0	6.82
5596	0	6.83

Table 6 Change in flame liftoff height (ΔH_L) with simulation corrected concentrations of $O_2(a^1\Delta_g)$ and O_3 present at flame for a plasma power of 80 Watts at 3.61 kPa.

$O_2(a^1\Delta_g)$ [ppm]	**O_3 [ppm]**	**ΔH_L [mm]**
10	423	7.70
2345	0	1.91
3285	0	5.64
3391	0	6.11

Table 7 Change in flame liftoff height (ΔH_L) with simulation corrected concentrations of $O_2(a^1\Delta_g)$ and O_3 present at flame for a plasma power of 80 Watts at 6.73 kPa.

The same O_2 loadings, flow rates, and pressures then were used on the plasma afterglow diagnostics system to find the concentrations of O_3 and $O_2(a^1\Delta_g)$ that were present at the lifted flame. The measured concentrations of O_3 and $O_2(a^1\Delta_g)$ were corrected for residence time using the kinetic model. The results are shown in **Table 6** and **Table 7** as a function of O_3 and $O_2(a^1\Delta_g)$ concentration for 3.61 kPa and 6.73 kPa, respectively. Overall, with NO addition, there was no change in the flow-field, temperature, or any species other than $O_2(a^1\Delta_g)$ when the plasma was cycled on and off. Turning on the plasma was the equivalent of introducing a pure source of

$O_2(a^1\Delta_g)$. The results in **Table 6** and **Table 7** show that there was a clear correlation between the concentration of $O_2(a^1\Delta_g)$ present and the change in flame liftoff height. **Figure 28** shows the trend of increasing change in flame liftoff height, hence flame speed enhancement, with increasing $O_2(a^1\Delta_g)$ concentration for both 3.61 kPa and 6.73 kPa. The experimental uncertainties for the change in flame liftoff height were ± 0.5 mm. For $O_2(a^1\Delta_g)$, the concentration uncertainty was ± 500 ppm, as shown by the error bars in **Fig. 28**.

With the results showing clearly the enhancement of flame propagation speed by $O_2(a^1\Delta_g)$, it was important to determine the enhancement quantitatively. Unlike the lifted flame at atmospheric pressure, a cold flow similarity solution does not describe the low-pressure experiments correctly; therefore, an indirect method was used to find the amount of flame speed enhancement quantitatively. The change in flame liftoff height shown in **Table 6**, **Table 7**, and **Fig. 28** indicates that approximately ten times the amount of $O_2(a^1\Delta_g)$ (approximately 5500 ppm) was needed to achieve the same enhancement as O_3 (approximately 500 ppm). Since the enhancement of flame propagation speed was established with the addition of O_3, it can be used to quantify the enhancement by $O_2(a^1\Delta_g)$. The C_2H_4 laminar and lifted flame speed enhancements were computed using the C_2H_4 kinetic mechanisms [65] with the addition of the O_3 reactions. The laminar and lifted flame speeds are related through the square root of the density ratio; therefore the, percent enhancements of the flame speeds were comparable. All of the experiments were performed for large flame liftoff heights where the mixture fraction gradient was small, and there was the closest agreement to the numerical simulations at a zero mixture fraction gradient. The lifted flame speed enhancement was used for comparison between experiments and numerical simulations. The results for the conditions of 500 ppm of O_3 addition at 3.61 kPa and 6.73 kPa showed approximately 1% enhancement of the lifted flame speed (**Fig. 29**). Since the flame liftoff height change for 500 ppm O_3 is equivalent to 5500 ppm $O_2(a^1\Delta_g)$, it was reasonable to assume that their effects on flame speed enhancement were comparable. The overall lifted flame speed enhancement would be higher because of the kinetic-induced hydrodynamic enhancement. If the effect of O_3 at low pressure is comparable to what was found at high pressure, then 5500 ppm of $O_2(a^1\Delta_g)$ will give approximately 2% to 3% enhancement of the lifted flame speed.

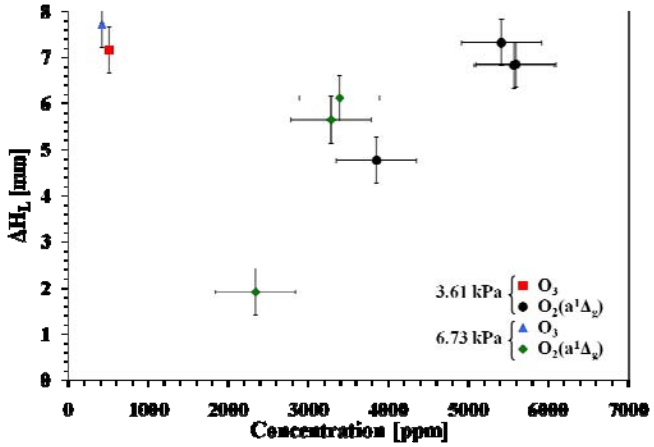

Fig.28 of experimental results of flame liftoff change with $O^2(a^1\Delta_g)$ and O_3 concentration for a plasma power of 80 Watts. The error bars denote the experimental uncertainties in the concentrations and change in flame liftoff height.

Reaction	Reaction Constant [cm^3/molecule/s]	Temperature Dependence	Activation Energy [kJ/mole]
Reactive Quenching of $O_2(a^1\Delta_g)$			
$H+O_2 \rightarrow O+OH$ [50]	$5.00x10^{-9}$	0	60.3
$H+O_2(a^1\Delta_g) \rightarrow O+OH$ [51]	$1.82x10^{-10}$	0	26.5
$H+O_2(a^1\Delta_g) \rightarrow O+OH$ [29]	$6.55x10^{-11}$	0	21.0
$OH+O_2(a^1\Delta_g) \rightarrow O+HO_2$ [51]	$2.16x10^{-11}$	0	141.4
$OH+O_2(a^1\Delta_g) \rightarrow H+O_3$ [51]	$7.31x10^{-17}$	1.44	226.4
$H_2+O_2(a^1\Delta_g) \rightarrow OH+OH$ [51]	$2.82x10^{-9}$	0	141.4
$H_2+O_2(a^1\Delta_g) \rightarrow HO_2+H$ [51]	$4.13x10^{-12}$	0	151.6
$H_2O+O_2(a^1\Delta_g) \rightarrow OH+HO_2$ [27]	$9.03x10^{-8}$	0.5	209.7
$H_2O+O_2(a^1\Delta_g) \rightarrow O+H_2O_2$ [27]	$2.05x10^{-12}$	0.5	283.5
Collisional Quenching of $O_2(a^1\Delta_g)$			
$H_2+O_2(a^1\Delta_g) \rightarrow H_2+O_2$ [52]	$2.16x10^{-13}$	0	21.6
$H_2+O_2(a^1\Delta_g) \rightarrow H_2+O_2$ [29]	$1.68x10^{-12}$	0	32.0
$H+O_2(a^1\Delta_g) \rightarrow H+O_2$ [51]	$6.97x10^{-16}$	0	0
$OH+O_2(a^1\Delta_g) \rightarrow OH+O_2$ [51]	$5.65x10^{-18}$	0	0
$HO_2+O_2(a^1\Delta_g) \rightarrow HO_2+O_2$ [51]	$5.65x10^{-18}$	0	0
$H_2O+O_2(a^1\Delta_g) \rightarrow H_2O+O_2$ [51]	$5.65x10^{-18}$	0	0
$H_2O_2+O_2(a^1\Delta_g) \rightarrow H_2O_2+O_2$ [51]	$5.65x10^{-18}$	0	0
Other Reactions with $O_2(a^1\Delta_g)$			
$H+HO_2 \rightarrow H_2+O_2(a^1\Delta_g)$ [51]	$3.32x10^{-12}$	0	2.4
$OH+O \rightarrow H+O_2(a^1\Delta_g)$ [51]	$9.63x10^{-12}$	0	51.8
$O_3+OH \rightarrow HO_2+O_2(a^1\Delta_g)$ [51]	$7.97x10^{-13}$	0	8.3
$O_3+HO_2 \rightarrow OH+O_2+O_2(a^1\Delta_g)$ [51]	$1.66x10^{-14}$	0	8.3
$HO_2+HO_2 \rightarrow H_2O_2+O_2(a^1\Delta_g)$ [51]	$1.49x10^{-11}$	0	4.2
$H_2O_2+O \rightarrow H_2O+O_2(a^1\Delta_g)$ [51]	$6.97x10^{-13}$	0	17.7

Table 8 Reaction rates of $O_2(a^1\Delta_g)$ with hydrogen containing species.

Numerical simulations were performed in order to explain the enhancement mechanism with the addition of $O_2(a^1\Delta_g)$. The C_2H_4 combustion mechanisms [65,66] with the O_3 reactions added were used along with the inclusion of $O_2(a^1\Delta_g)$ reactions. The reactive and collisional quenching rates of $O_2(a^1\Delta_g)$ with oxygen and inert species as functions of temperature have been well studied and were used to compute the cold flow transport of $O_2(a^1\Delta_g)$ in the ICOS system and prior to the flame in the combustion system. These $O_2(a^1\Delta_g)$ reactions were added to the C_2H_4/O_3 mechanisms. The reactions of $O_2(a^1\Delta_g)$ with the fuel also have been well studied at 298 K, but there are little data at intermediate and high temperatures. The most studied $O_2(a^1\Delta_g)$ reactions applicable to a combustion system are for H_2-O_2 mixtures. These reactions of hydrogen and oxygen containing species with $O_2(a^1\Delta_g)$ are shown in **Table 8** and have been compiled specifically for H_2-O_2 mixtures activated by plasma. The rates were taken from previous numerical work on plasma-assisted H_2-O_2 combustion systems, as well as from specific reaction rate studies [67,68,69]. A few differences arose, specifically regarding the two reactions

$$H + O_2\left(a^1\Delta_g\right) \rightarrow O + OH \tag{18}$$

$$H_2 + O_2\left(a^1\Delta_g\right) \rightarrow H_2 + O_2 . \tag{19}$$

The reactions were added to the C_2H_4/O_3 kinetic mechanisms and the results are shown in **Fig. 29** using the concentrations of O_3 and $O_2(a^1\Delta_g)$ from the experiments. The results of enhancement using the $O_2(a^1\Delta_g)$ concentrations found in the experiments showed flame speed enhancement of more than 5%. When compared to the experimental results of lifted flame speed enhancement by O_3 (that was found to be approximately 1%) there was a large discrepancy, which was well outside the uncertainties for the system. For example, in the experiments at 3.61 kPa, the change in flame liftoff height for 500 ppm O_3 was approximately equal to 5500 ppm $O_2(a^1\Delta_g)$ **(Fig. 28).** According to the numerical simulations, there was more than a factor of five difference in the enhancement of flame speed. Considering that the O_3 and $O_2(a^1\Delta_g)$ both should enhance the lifted flame speed similarly with the lean and rich enhancement more than for stoichiometric mixtures, there is a significant error in the $O_2(a^1\Delta_g)$ kinetic calculations. With regard to the differences in the rates for reactions, the deviations in the flame speed enhancement were no more than ± 4%. The vertical error bars in **Fig. 29** show the negligible enhancement differences when using the two published rates for reactions, [18] and [19]; therefore, the sensitivity of the flame speed to the differences in reaction rates do not account for the significant deviations from the experiments.

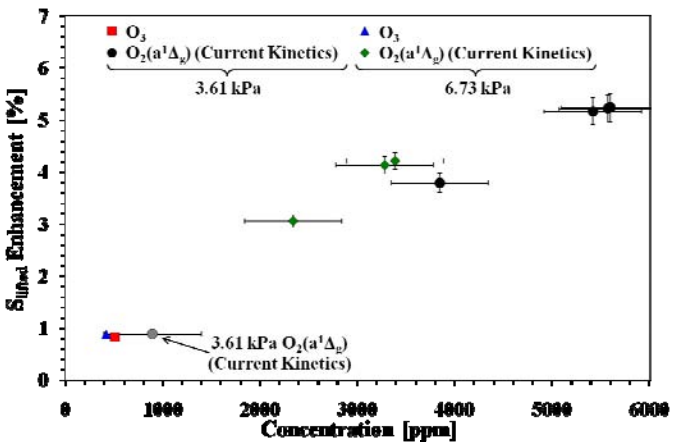

Fig.29 Plot of computational results of lifted flame speed enhancement with $O_2(a^1\Delta_g)$ and O_3. The horizontal error bars denote the propagation of uncertainty from the concentrations found experimentally, while the vertical error bars denote the range of lifted flame speed enhancement when using the different published reaction rates.

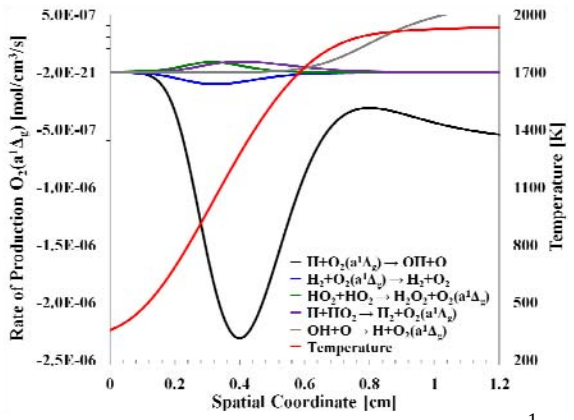

Fig.30 Rate of production plot of $O_2(a^1\Delta_g)$ superimposed on the temperature profile showing the major consumption pathways of $O_2(a^1\Delta_g)$ with current published rate data with hydrogen containing species.

To understand what caused the significant flame speed enhancement by $O_2(a^1\Delta_g)$, a rate of production plot of $O_2(a^1\Delta_g)$ in the flame is shown in **Fig. 30**. The major consumption pathways of $O_2(a^1\Delta_g)$ were from the branching reaction with H, with some contribution of collisional quenching by H_2. The reaction of $O_2(a^1\Delta_g)$ with H will enhance the flame significantly, since it is a primary radical branching reaction. It was reasonable that the enhancement was so large in the numerical simulations.

The changes in the radical pool in the earlier stages of the flame are shown in **Fig. 31**. In the earlier stages of the flame where the temperature is elevated slightly between 400 K and 500 K, the $O_2(a^1\Delta_g)$ begins to be consumed, causing a decrease in the C_2H_4 concentration and a subsequent increase in O and OH. The increase in concentration of OH would provide chemical heat release through subsequent reactions earlier in the flame to enhance the overall flame speed significantly. The higher concentrations of OH in the earlier stages of the flame leading to chemical heat release and enhanced flame speed were shown through the study of O_3 addition. The increase in the radical pool concentration of O from the reactions with $O_2(a^1\Delta_g)$ were investigated in greater depth through a rate-of-production analysis. The results showed that the major pathway for O consumption was from the reaction with the parent fuel, C_2H_4, and its fragment, CH_3. The end results of flame propagation enhancement came from the increased radical pool concentration and extraction of chemical heat release earlier in the flame compared to the results with no $O_2(a^1\Delta_g)$ addition. **Figure 32** clearly indicates the elevated levels of chemical heat release by showing the total volumetric heat release as a function of temperature in the flame. There is significantly more heat release between 800 K and 1500 K with $O_2(a^1\Delta_g)$ addition, which aligns well with the peak consumption of $O_2(a^1\Delta_g)$ and elevated radical concentrations, shown in **Fig. 30** and **Fig. 31**, respectively.

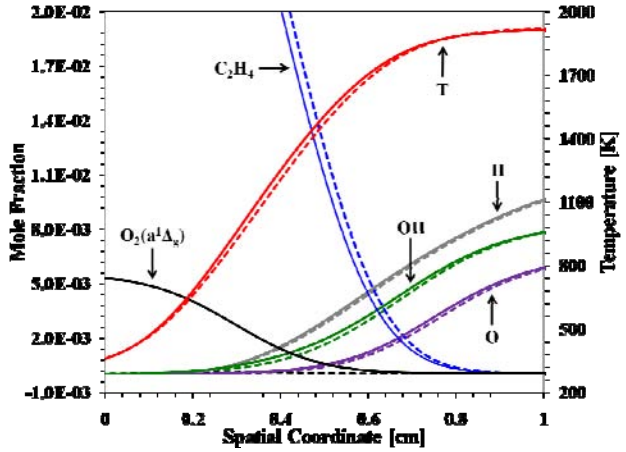

Fig.31 Temperature and mole fraction profiles, dashed lines = w/o $O_2(a^1\Delta_g)$, solid lines = w/ $O_2(a^1\Delta_g)$.

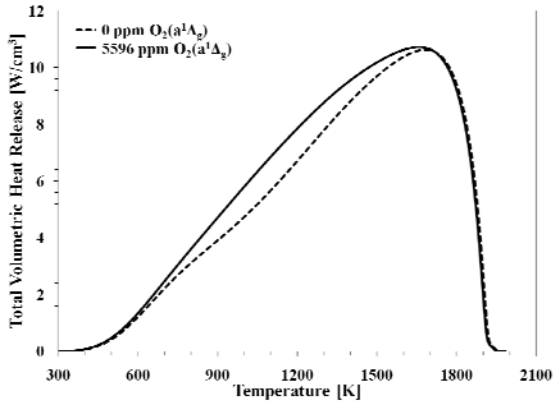

Fig.32 Heat release versus temperature showing elevated levels of chemical heat release at lower temperatures with $O_2(a^1\Delta_g)$ addition.

With an understanding of how $O_2(a^1\Delta_g)$ enhanced the flame speed in the numerical simulations, it becomes apparent that there are two possible explanations for the discrepancy shown in **Fig. 29** with respect to the enhancement by O_3 and $O_2(a^1\Delta_g)$. First, a significant concentration of the $O_2(a^1\Delta_g)$ could quench before reacting with H. The collisional quenching reactions of $O_2(a^1\Delta_g)$ with the parent fuel or its fragments could decrease the concentration significantly, thereby leading to less enhancement. To achieve the same enhancement of $O_2(a^1\Delta_g)$ as the calculations with O_3 indicate, approximately 900 ppm $O_2(a^1\Delta_g)$ would be needed (shown in **Fig. 29** for 3.61 kPa). Approximately 4600 ppm of $O_2(a^1\Delta_g)$ would have to quench

collisionally, allowing only a small fraction of the original concentration to react with H. The enhancement would be less, especially if the dominating reactions of $O_2(a^1\Delta_g)$ would be with the parent fuel and not providing chain branching as in the reaction of H with $O_2(a^1\Delta_g)$. Second, there could be a combination of reactive and collisional quenching pathways for $O_2(a^1\Delta_g)$ that could be responsible for the enhancement observed in the experiments.

Reaction	Reaction Constant [cm^3/molecule/s]	Temperature Dependence	Activation Energy [kJ]
$CH_4+O_2(a^1\Delta_g) \rightarrow CH_4+O_2$ [42]	$1.40x10^{-18}$	0	0
$CH_4+O_2(a^1\Delta_g) \rightarrow CH_3+HO_2$ [54]	$6.14x10^{-12}$	0	149.0
$C_2H_4+O_2(a^1\Delta_g) \rightarrow C_2H_4+O_2$ [*low]	$7.71x10^{-16}$	0	15.0
$C_2H_4+O_2(a^1\Delta_g) \rightarrow C_2H_4+O_2$ [*high]	$3.12x10^{-13}$	0	30.0
$C_2H_4+O_2(a^1\Delta_g) \rightarrow C_2H_4+O_2$ [* exp. fit]	$5.46x10^{-10}$	0	48.6
$C_2H_4+O_2(a^1\Delta_g) \rightarrow C_2H_3+HO_2$ [*]	$7.01x10^{-11}$	0	146.5

Table 9 Reaction rates of $O_2(a^1\Delta_g)$ with hydrocarbon species. [*low] = estimated rate with low activation energy, [*high] = estimated rate with high activation energy, [*exp. fit] = estimated rate with activation energy to fit trend of experimental results, [*] = estimated rate.

The reactive and collisional quenching rates for some of the hydrocarbon species were added to the kinetic mechanism one at a time to test the sensitivity of flame speed enhancement. In **Table 9** is a list of the reactions along with their rates. Initially the reactions with CH_4 of

$$CH_4 + O_2\left(a^1\Delta_g\right) \rightarrow CH_4 + O_2 \tag{20}$$

$$CH_4 + O_2\left(a^1\Delta_g\right) \rightarrow CH_3 + HO_2 \tag{21}$$

were added but did not change the flame speed enhancement, which was reasonable considering the low concentrations of CH_4 in the system. Next, noting that the inclusion of $O_2(a^1\Delta_g)$ collisional quenching by the parent fuel H_2 in an H_2-O_2 system via reaction (18) was found in previous numerical investigations to be significant and decreased the effectiveness of $O_2(a^1\Delta_g)$ enhancement, it is reasonable to include collisional quenching by the parent fuel via

$$C_2H_4 + O_2\left(a^1\Delta_g\right) \rightarrow C_2H_4 + O_2 \tag{22}$$

for our hydrocarbon fueled combustion system. Some collisional reaction rates for $O_2(a^1\Delta_g)$ with C_2H_4 and other small hydrocarbon fuels are known, but they are only at 298 K. To the authors knowledge, there are no verified quenching rates of hydrocarbon species (specifically C_2H_4) with $O_2(a^1\Delta_g)$ in the intermediate- to high-temperature range where they would be the most important for a flame system.

The work of Borrell and Richards found that the temperature dependence of $O_2(a^1\Delta_g)$ quenching by H_2 was approximately Arrhenius and that other species also follow an Arrhenius temperature dependence [69]. It was assumed that C_2H_4 might also follow this temperature dependence for quenching $O_2(a^1\Delta_g)$. Originating with the quenching rate of $O_2(a^1\Delta_g)$ by C_2H_4 at 298 K, an Arrhenius temperature-dependent rate was estimated to explain the trend discrepancy shown in the experimental results of **Fig. 29**. Three different temperature dependencies were chosen with a range of activation energies. Previously published temperature-dependent collisional quenching rates of $O_2(a^1\Delta_g)$ have shown that the activation energy range is typically

between 15 kJ/mole and 20 kJ/mole [55]. The activation energy for the collisional quenching of $O_2(a^1\Delta_g)$ by H_2 is as high as 32 kJ/mole; therefore, the range of 15-30 kJ/mole was chosen for the activation energies of reaction (21), with a reaction constant chosen in order to agree with published rates at 298 K. The envelope of reaction rates for reaction (22) using activation energies from 15 kJ/mole to 30 kJ/mole are shown in **Fig. 33** and are labeled as "Quenching A."

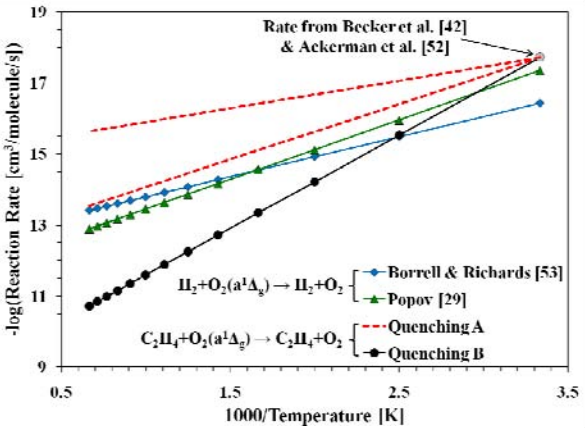

Fig.33 temperature dependent collisional quenching rates of $O_2(a1\Delta g)$ by H_2 and C_2H_4. The rates with C_2H_4 are estimates.

Computations were performed using the rates within the envelope of "Quenching A" in **Fig. 33**, and the results are shown in **Fig. 34**. The flame speed enhancement decreased slightly but not enough to explain the discrepancy. In an attempt to explain the disagreement, a rate for reaction (20) was chosen in order to bring the enhancement by $O_2(a^1\Delta_g)$ down to the enhancement by O_3. To match this result, a reaction constant of 5.46 x 10^{-10} cm^3/molecule/s and an activation energy of 48.6 kJ/mole were chosen, with the temperature dependence shown in **Fig. 33** as "Quenching B." By using the "Quenching B" rate for reaction (22), the results of enhancement by O_3 and $O_2(a^1\Delta_g)$ were approximately equal, thereby agreeing with the trends of the experimental results (**Fig. 34**). A rate of production analysis of $O_2(a^1\Delta_g)$ was performed with the "Quenching B" rate and the major consumption pathway shifted to reaction (22) with negligible consumption by reaction (18). The concentration profile of $O_2(a^1\Delta_g)$ showed a more rapid decrease in the earlier stages of the flame but with no appreciable increase in C_2H_4 consumption or O and OH production. Furthermore, the quenching pathway involved electronic-to-vibrational-translational energy transfer that releases so little energy that the translational temperature changed negligibly. The computed temperature profiles confirmed the negligible increase in temperature and therefore that a significant concentration of

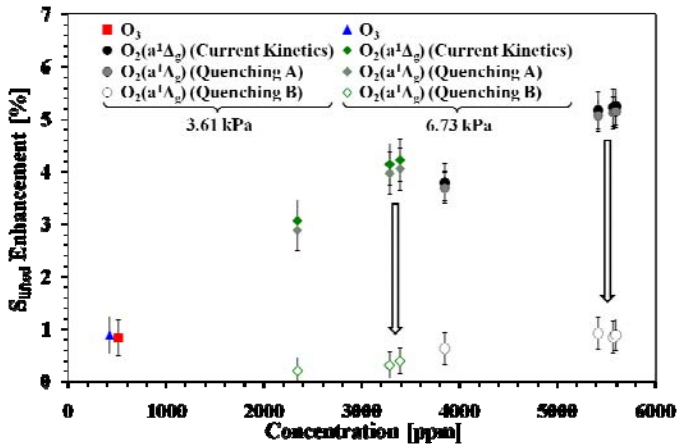

Fig.34 of computational results of lifted flame speed enhancement with $O_2(a^1\Delta_g)$ and O_3 using the estimated collisional quenching rate of C2H4 with $O_2(a^1\Delta_g)$ from Fig. 31. "Quenching A" = inclusion of temperature dependent quenching of $O_2(a^1\Delta_g)$ by C_2H_4 with Ea=30 kJ/mol, "Quenching B" = inclusion of temperature dependent quenching of $O_2(a^1\Delta_g)$ by C2H4 to fit trend of experimental results. The error bars denote the variation in lifted flame speed enhancement when using different C_2H_4 kinetic mechanisms.

$O_2(a^1\Delta_g)$ was consumed and did not affect the flame in the process. The high activation energy and hence strong temperature dependence of reaction (22), given by the estimated rate "Quenching B," mitigated the computed enhancement discrepancy, but the rate appears unreasonably high and has not been validated and therefore requires further investigations.

The last possible explanation of the trend discrepancy in computed enhancement lies in the reactive quenching of $O_2(a^1\Delta_g)$ by C_2H_4 and its fragments. The first assumption was to decrease the activation energy of the reaction

$$C_2H_4 + O_2\left(a^1\Delta_g\right) \rightarrow C_2H_3 + HO_2 \tag{23}$$

by the energy contained within $O_2(a^1\Delta_g)$. This assumption equates to decreasing the activation energy by 0.98 eV (94.5 kJ/mole), and the rate is shown in **Table 9**. The inclusion of this reaction in the kinetic mechanism did not result in any change in flame speed enhancement because the rate is slow in comparison to other reaction pathways with C_2H_4 and $O_2(a^1\Delta_g)$. Beyond reaction (23) there could be other possible product pathways that have been investigated through quantum calculations with C_2H_4 [70,71]. The pathways show that $O_2(a^1\Delta_g)$ can attack the double carbon bond to split the parent fuel molecule, possibly providing significant enhancement of fuel oxidation rates by producing CH_2O and other hydrocarbon fragments, but the rates are not known.

The results suggest that the probable reactive scheme has both collisional and reactive quenching of $O_2(a^1\Delta_g)$ by the parent fuel and its fragments. There remain many unknowns as to the kinetic mechanisms for $O_2(a^1\Delta_g)$ with hydrocarbons under flame conditions. The lack of rate data for these reactions in the intermediate- to high-temperature range that is applicable to combustion systems remains a significant obstacle and requires further investigation; nevertheless, the results from this investigation have provided the first experimental data set for flame propagation enhancement by $O_2(a^1\Delta_g)$ that provides a foundation for future investigations.

2.3.3 Conclusions

The present study provides a promising approach to isolate plasma-produced excited species for the kinetic study of plasma-assisted combustion. By separating the plasma and combustion systems, specific plasma-produced species can be isolated and measured while minimizing the complications of other plasma-flame interactions. Isolation of the specific effects of individual plasma-produced species will have a significant impact on the development of detailed plasma-flame kinetic mechanisms. Through the current work a platform to study quantitatively the enhancement effects of plasma-produced $O_2(a^1\Delta_g)$ on C_2H_4 lifted flame propagation speeds was developed. It was found quantitatively, for the first time, that $O_2(a^1\Delta_g)$ enhances flame propagation. The addition of NO to the plasma afterglow allowed for an order-of-magnitude increase in the $O_2(a^1\Delta_g)$ concentration at a given residence time by removing the quenching species O_3 and O. The NO was extremely effective because of the catalytic cycle to remove O_3 and O, as well as having a negligible effect on flame speed. The $O_2(a^1\Delta_g)$ was produced in concentrations of over 5000 ppm to enhance flame propagation of C_2H_4 lifted flames by several percent at 3.61 kPa and 6.73 kPa pressures.

Numerical simulations using the state-of-the-art rates of the collisional and reactive quenching reactions have shown that there is a significant discrepancy in the predicted enhancement compared with the experimental data. The pathways of enhancement found in the simulations showed that the branching reaction of $O_2(a^1\Delta_g)$ with H provided O and OH early in the reaction zone and increased chemical heat release and flame propagation speed. The lack of temperature-dependent quenching rate data of $O_2(a^1\Delta_g)$ by hydrocarbon species was suspected to

be the main cause for the discrepancy. Estimations of the temperature dependent collisional quenching rate of $O_2(a^1\Delta_g)$ by C_2H_4 have shown good agreement with the experimental results trends, but the suggested rates appear unreasonably high and need to be validated in future studies. The reactive quenching pathways and their rates remain unknown; therefore, a combination of both the collisional and reactive quenching rates of $O_2(a^1\Delta_g)$ with hydrocarbon species, specifically the parent fuel molecule, are required in order to explain combustion enhancement correctly. The experimental results therefore have provided the first data of the isolated effect of $O_2(a^1\Delta_g)$ under flame conditions, which are of paramount importance for the development of reaction pathways and plasma-flame kinetic mechanisms. Future investigations are being targeted at establishing temperature-dependent quenching rates of $O_2(a^1\Delta_g)$ to enable more accurate predictive modeling of the plasma-flame interaction.

The experimental results also imply that when energy is coupled into specific plasma-produced species, there is no requirement for the control of heat loss. If energy is coupled into a reactive flow to raise the translational gas temperature only, there needs to be careful thermal management. When energy is coupled into energy modes of specific species, no thermal management needs to be considered. The energy contained within the species can be transported for significant distances and residence times and can be extracted at the combustion reaction zone. The plasma power remained constant at 80 W for all conditions with O_3 and/or $O_2(a^1\Delta_g)$ in the current experiments; therefore, the energy coupled into the flow by the plasma was recovered at the flame. More $O_2(a^1\Delta_g)$ was produced than O_3 for the same plasma power because of the difference in energy to produce these species.

Lastly, in and immediately downstream of an oxygen plasma there would be both O and $O_2(a^1\Delta_g)$ but no O_3 since it is the product of a time-dependent recombination of O and O_2. The O atoms most likely will be more reactive, but there will be higher concentrations of $O_2(a^1\Delta_g)$. If oxygen plasma is located closer to a combustion reaction zone, the effects of $O_2(a^1\Delta_g)$ can become more pronounced.

3.0 Participating Personnel

Princeton University:

Fully or Partially Supported by the Project:	Professor Yiguang Ju, PI
	Timothy Ombrello, graduate student
	Zheng Chen, graduate student
	Sanghee Won, Research staff
	Jingning Shan, Research staff

Drexel University:

Fully or Partially Supported by the Project:	Professor Alexander Fridman, co-PI
	Professor Alexander Gutsol
	Shailesh Gangoli, graduate student

4.0 Publications

Peer Reviewed Journal Publications

1. Ombrello, T., Ju, Y., and Fridman, A., "Kinetic Ignition Enhancement of Diffusion Flames by Nonequilibrium Magnetic Gliding Arc Plasma," *AIAA Journal*, Vol. 46, No. 10, 2008, pp. 2424-2433.
2. Fridman, A., Gutsol, A., Gangoli, S., Ju, Y., and Ombrello, T., "Characteristics of Gliding Arc and its Application in Combustion Enhancement," *Journal of Propulsion and Power*, Vol. 24, No. 6, 2008, pp. 1216-1228.
3. Ombrello, T. and Ju, Y., "Kinetic Ignition Enhancement of H_2 versus Fuel-Blended Air Diffusion Flames Using Nonequilibrium Plasma," *IEEE Transactions on Plasma Science*, Vol. 36, No. 6, 2008, pp. 2924-2932, also presented at the 32nd Symp. Combustion.
4. Timothy Ombrello, Sang Hee Won, and Yiguang Ju, and Skip Williams, Flame Propagation Enhancement by Plasma Excitation of Oxygen Part I: Effects of O_3,*Combustion and Flame*, in press, 2010.
5. Timothy Ombrello, Sang Hee Won, and Yiguang Ju, and Skip Williams, Flame Propagation Enhancement by Plasma Excitation of Oxygen Part II: Effects of $O_2(a^1\Delta_g)$, *Combustion and Flame*, in press, 2010.
6. Zheng Chen, Michael P. Burke, Yiguang Ju, Effects of Lewis Number and Ignition Energy on the Determination of Laminar Flame Speed Using Propagating Spherical Flames, *Proc. Combust. Institute*, Volume 32, Issue 1, 2009, Pages 1253-1260.

Presentations at Conferences

1. Ombrello, T., Ju, Y., and Fridman, A., "Investigation of Non-Equilibrium Plasma Induced Kinetic Ignition of Counterflow Diffusion Flames," AIAA-2008-1361, 46th AIAA Aerospace Sciences Meeting and Exhibit, 7-10 January 2008, Reno, Nevada.
2. Chen, Z., Burke, M., and Ju, Y., "Effects of Lewis Number on Spherical Flame Initiation," AIAA-2008-977, 46th AIAA Aerospace Sciences Meeting and Exhibit, 7-10 January 2008, Reno, Nevada.
3. Ombrello, T. and Ju, Y., "Studies of Ignition Enhancement Mechanisms of H_2 Versus Fuel-Blended-Air Diffusion Flames Using Non-Equilibrium Plasma," 32nd International Symposium on Combustion, The Combustion Institute, 3-8 August 2008, Montreal, Quebec, Canada.
4. Ombrello, T., Won, S.H., and Ju, Y., "Lifted Flame Speed Enhancement by Ozone," 4th International Workshop on Plasma-assisted Combustion, 16-19 September 2008, Falls Church, Virginia.
5. Ombrello, T., Won, S.H., Ju, Y., and Williams, S., "Lifted Flame Speed Enhancement by Plasma Excitation of Oxygen," AIAA-2009-0689, 47th AIAA Aerospace Sciences Meeting, 5-8 January 2009, Orlando, Florida.
6. Chen, Z., Burke, M., and Ju, Y., "Studies on the Critical Flame Radius and Minimum Ignition Energy for Spherical Flame Initiation," AIAA-2009-1184, 47th AIAA Aerospace Sciences Meeting, 5-8 January 2009, Orlando, Florida.
7. Zheng Chen, Michael Burke, Yiguang Ju, "Studies on the Critical Flame Radius and Minimum Ignition Energy for Spherical Flame Initiation," AIAA-2009-1184,47th AIAA Aerospace Sciences Meeting, 2009.
8. Timothy Ombrello, Sang Hee Won,Yiguang Ju, "Enhancement of flame speed by plasma excitation of oxygen," Proceedings of the 6th U.S. National Combustion Meeting, 2009.
9. Timothy Ombrello, Wenting Sun, Sang Hee Won, Yiguang Ju, Skip Williams, Kihei, Maui, Campbell Carter, "Mechanisms of Kinetic Combustion Enhancement by O2(a1Δg, AIAA-2010-1586, 48th AIAA Aerospace Sciences Meeting, 2010.

10. Wenting Sun, Timothy Ombrello, Sang Hee Won, Mruthunjaya Uddi, Yiguang Ju, “Effects of Non-Equilibrium Plasma on Counterflow Diffusion Flames,” AIAA-2010-1331, 48th AIAA Aerospace Sciences Meeting, 2010.

5.0 Interactions and Consultations

Professor Ju and Timothy Ombrello have been in collaboration with Professor Fridman and his associates Professor Gutsol and Shailesh Gangoli at the Drexel Plasma Institute of Drexel University on a regular basis. This interaction has allowed for a discussion and work forum to take the knowledge obtained via the analysis of the MGA plasma discharge and apply it to the knowledge of combustion to develop a model of the plasma/flame interaction.

Professor Ju, Dr. Sanghee Won and Timothy Ombrello have also worked with Dr. Skip Williams of the Air Force Research Laboratory at Wright-Patterson Air Force Base to design and develop a low pressure chamber to be used for combustion experiments to examine the effects of O_3 and singlet oxygen via the microwave plasma discharge on the flame propagation of hydrocarbon lifted flames.

Professor Ju and Timothy Ombrello have also worked closely with Dr. Campbell Carter of the Air Force Research Laboratory at Wright-Patterson Air Force Base to establish diagnostic capability of atomic oxygen measurements. Timothy Ombrello and Sanghee Won have traveled to Wright-Paterson Air Force Base twice to perform laser diagnostic measurements of OH PLIF, ozone, and singlet oxygen.

6.0 Honors and Awards

May 2007 Best Paper Award, The paper "Flammability Limit Extension of Non-Premixed Counterflow Flames via Stabilized Non-Equilibrium Plasma Gliding Arc" by T. Ombrello, X. Qin, Y. Ju and C. Carter and presented by my graduate student (T. Ombrello) at the Fifth Asia Pacific Conference on Combustion held at Adelaide of Australia in 2005, won the most outstanding paper prize for young researchers (the Young Investigator Award).

July 2008 Zheng Chen, awarded the Bernard Lewis Fellowship from the International Combustion Institute

Tim Ombrello, the Wu Prize for Excellence in Research of Princeton University.

7.0 Inventions

NA

8.0 References of This Report

1 E. Barbi, J. Mahan, W. O'Brien, T. Wagner, J. Prop. Power 5:2 (1989) 129-133.

2 I. Kimura, H. Aoki, M. Kato, Combust. Flame 42 (1981) 297-305.

3 K. Takita, A. Moriwaki, T. Kitagawa, G. Masuya, Combust. Flame 132:4 (2003) 679-689.

4 T. Wagner, W. O'Brien, G. E. Northam, J. Prop. Power 5:5 (1989) 548-554.

5 T. Ombrello, X. Qin, Y. Ju, A. Gutsol, A. Fridman, AIAA J. 44:1 (2006) 142-150.

6 T. Ombrello, Y. Ju, A. Fridman, AIAA J. 46:10 (2008) 2424-2433.

7 T. Ombrello, Y. Ju, IEEE Trans. Plasma Sci. 36:6 (2008) 2924-2932.

8 S. Bozhenkov, S. Starikovskaia, A. Y. Starikovskii, Combust. Flame 133 (2003) 133-146.

9 A. Starikovskii, Proc. Combust. Inst. 30 (2005) 2405-2417.

10 G. Lou, A. Bao, M. Nishihara, S. Keshav, Y. Utkin, J. Rich, W. Lempert, I. Adamovich, Proc. Combust. Inst. 31 (2007) 3327-3334.

11 S. Pancheshnyi, D. Lacoste, A. Bourbon, C. Laux, IEEE Trans. Plasma Sci. 34:6 (2006) 2478-2487.

12 H. Jagers, A. Von Engel, Combust. Flame 16 (1971) 275-285.

13 S. Won, M. Cha, C. Park, S. Chung, Proc. Combust. Inst. 31 (2007) 963-970.

14 S. Won, S. Ryu, M. Kim, M. Cha, S. Chung, Combust. Flame 152 (2008) 496-506.

15 I. Esakov, L. Grachev, K. Khodatev, V. Vinogradov, D. Van Wie, 44th AIAA Aerospace Sciences Meeting and Exhibit (2006) AIAA-2006-1212.

16 Y. Ju, S. Macheret, R. Miles, D. Sullivan, 40th AIAA/ASME/SAE/ASEE Joint Propulsion Conference and Exhibit (2004) AIAA-2004-2721.

17 S. Zaidi, S. Macheret, L. Vasilyak, R. Miles, Y. Ju, D. Sullivan, 35th AIAA Plasmadynamics and Lasers Conference (2004) AIAA-2004-3707.

18 C. Cathey, J. Cain, H. Wang, M. Gunderson, C. Carter, M. Ryan, Combust. Flame 154 (2008) 715-727.

19 I. Kosarev, N. Aleksandrov, S. Kindysheva, S. Starikovskaia, A. Starikovskii, J. Prop. Power 24:6 (2008) 1182-1197.

20 E. Stockman, S. Zaidi, R. Miles, C. Carter, M. Ryan, Combust. Flame 156 (2009) 1453-1461.

21 S. Starikovskaia, J. Phys. D: Appl. Phys. 39 (2006) R265-R299.

22 M. Uddi, N. Jiang, E. Mintusov, I. Adamovich, W. Lempert, Proc. Combust. Inst. 32 (2009) 929-936.

23 V. Golovitchev, J. Chomiak, Combust. Sci. Tech. 135:1-6 (1998) 31-47.

24 H. Nishida, T. Tachibana, J. Prop. Power 22:1 (2006) 151-157.

25 T. Nomaguchi, S. Koda, Proc. Combust. Inst. 22:1 (1988) 1677-1682.

26 T. Tachibana, H. K, H. Nishida, H. Osada, Combust. Flame 85:3-4 (1991) 515-519.

27 H. Yamada, M. Yoshii, A. Tezaki, Proc. Combust. Inst. 30:1 (2005) 2773-2780.

28 D. Lucas, D. Dunn-Rankin, K. Hom, N. Brown, Combust. Flame 69:2 (1987) 171-184.

29 B. Lukhovitskii, A. Starik, N. Titova, Combust. Expl. Shock Waves 41:4 (2005) 386-394.

30 A. Starik, B. Lukhovitsky, N. Titova, J. Russian Laser Research 27:6 (2006) 533-551.

31 M. Gluckstein, R. Morrison, T. Khammash, (1955) Combustion with Ozone-Modification of Flame Speeds C2 Hydrocarbon-Air Mixtures, University of Michigan.

32 A.A. Ionin, I.V. Kochetov, A.P. Napartovich, N.N. Yuryshev, J. Phys. D: Appl. Phys. 40 (2007) R25-R61.

33 A. Starik, N. Titova, Kinet. Catal. 44:1 (2003) 28-39.

34 A. Starik, N. Titova, L. Bezgin, V. Kopchenov, V. Naumov, Czech. J. Phys. 56 (2006) B1357-B1363.

35 A. Starik, N. Titova, L. Bezgin, V. Kopchenov, V. Naumov, Czech. J. Phys. 56 (2006) B1357-B1363.

36 A. Starik, P. Kuleshov, N. Titova, Tech. Phys. 53:2 (2008) 235-243.

37 V. Kozlov, A. Starik, N. Titova, Combust. Expl. Shock Waves 44:4 (2008) 371-379.

38 A. Bourig, D. Thevenin, J. Martin, G. Janiga, K. Zahringer, Proc. Combust. Inst. 32 (2009) 3171-3179.

39 G. Smekhov, L. Ibraguimova, S. Karkach, O. Skrebkov, O. Shatalov, High Temp. 45:3 (2007) 395-407.

40 G. Smekhov, L. Ibraguimova, S. Karkach, O. Skrebkov, O. Shatalov, High Temp. 45:3 (2007) 395-407.

41 O. Skrebkov, S. Karkach, Kinet. Catalysis 48:3 (2007) 367-375.

42 V. Smirnov, O. Stelmakh, V. Fabelinsky, D. Kozlov, A. Starik, N. Titova, J. Phys. D - Appl. Phys. 41:19 (2008) .

43 A. Starik, B. Lukhovitskii, V. Naumov, N. Titova, Tech. Phys. 52 (2007) 1281-1290.

44 A. Starik, N. Titova, Doklady Phys. 46 (2001) 627-632.

45 Li, J., Zhao, Z., Kazakov, A., and Dryer, F.L., “An Updated Comprehensive Kinetic Model of Hydrogen Combustion,” International Journal of Chemical Kinetics, 36 (2004) 1-10.

46 Mueller, M.A., Yetter, R.A. and Dryer, F.L., “Kinetic Modeling of the CO/H2O/O2/NO/SO2 System: Implications for High-Pressure Fall-off in the SO2 + O(+M) = SO3(+M) Reaction,” International Journal of Chemical Kinetics, 30 (2000) 317-339.

47 Zhao, Z., Chaos, M., Kazakov, A., and Dryer, F.L., “Thermal Decomposition Reaction and a Comprehensive Kinetic Model of Dimethyl Ether,” International Journal of Chemical Kinetics, 40 (2008) 1-18.

48 Bowman et al., GRI-Mech Homepage, Gas Research Institute, Chicago, 1994, URL:http://www.me.berkeley.edu/gri_mech/.

49 Chen, Z., Qin, X., Ju, Y., Zhao, Z., Chaos, M., and Dryer, F.L., “High Temperature Ignition and Combustion Enhancement by Dimethyl Ether Addition to Methane-Air Flames,” Proceedings of the Combustion Institute, Thirty-First International Symposium on Combustion, 31 (2007) 1215-1222.

50 Langille, J.A., Dong, Y., Andac, M.G., Egolfopoulos, F.N., and Tsotsis, T.T., “Non-Premixed Ignition by Vitiated Air in Counterflow Configurations,” Combustion Science and Technology, 178:4 (2006) 635-653.

51 J. Malicet, D. Daumont, J. Charbonnier, C. Parisse, A. Chakir, J. Brion, J. Atm. Chem. 21:3 (1995) 263-273.

52 S. Chung, Proc. Combust. Inst. 31:1 (2007) 877-892.

53 S. Chung, Proc. Combust. Inst. 31:1 (2007) 877-892.

54 J. Lee, S. Won, S. Jin, S. Chung, Combust. Flame 135:4 (2003) 449-462.

55 Y. Ju, Y. Xue, Proc. Combust. Inst. 30 (2005) 295-301.

56 Y. Xue, Y. Ju, Combust. Sci. Tech. 178 (2006) 2219-2247.

57 M. Kim, S. Won, S. Chung, Proc. Combust. Inst. 31 (2007) 901-908.

58 G. Ruetsch, L. Vervisch, A. Linan, Phys. Fluids 7 (1995) 1447-1454.

59 PREMIX from the CHEMKIN Package, Reaction Design, 6440 Lusk Boulevard, Suite D-205 San Diego, CA 92121, www.reactiondesign.com.

60 L. Ibraguimova, G. Smekhov, O. Shatalov, Recommended Rate Constants of Chemical Reactions in an H2-O2 Gas Mixture with Electronically Excited Species O2(1Δ), O(1D), OH(2Σ) Involved, Institute of Mechanics of Lomonosov, Moscow State University (2003).

61 G. Smekhov, L. Ibraguimova, S. Karkach, O. Skrebkov, O. Shatalov, High Temp. 45:3 (2007) 395-407.

62 Z. Qin, V. Lissianski, H. Yang, W. Gardiner, S. Davis, H. Wang, Proc. Combust. Inst. 28:2 (2000) 1663-1669.

63 R. Morrissey, C. Schubert, Combust. Flame 7:3 (1963) 263-268.

64 S. Williams, M. Gupta, T. Owano, D. Baer, A. O'Keefe, D. Yarkony, S. Matsika, Opt. Lett. 29:10 (2004) 1066-1068.

65 H. Wang, A. Laskin, Internal Report, 1998.

66 H. Wang, X. You, A.V. Joshi, S.G. Davis, A. Laskin, F. Egolfopoulos, C.K. Law, USC Mech Version II. High-Temperature Combustion Reaction Model of H2/CO/C1-C4 Compounds, http://ignis.usc.edu/USC_Mech_II.htm, May 2007.

67 L. Ibraguimova, G. Smekhov, O. Shatalov, Recommended Rate Constants of Chemical Reactions in an H2-O2 Gas Mixture with Electronically Excited Species O2(1Δ), O(1D), OH(2Σ) Involved, Institute of Mechanics of Lomonosov, Moscow State University (2003).

68 R.A. Ackerman, J.N. Pitts, R.P. Steer, J. Chem. Phys. 52 (1970) 1603-1604.

69 P. Borrell, D.S. Richards, J. Chem. Soc., Faraday Trans. 2 85:9 (1989) 1401-1411.

70 M. Hotokka, B. Roos, P. Siegbahn, J. Amer. Chem. Soc. 105:16 (1983) 5263-5269.

71 Y. Yoshioka, T. Tsunesada, K. Yamaguchi, I. Saito, International J. Quant. Chem. 65 (1997) 787-801.